



Title	Dynamical downscaling of future sea level change in the western North Pacific using ROMS
Author(s)	Liu, Zhao-Jun; Minobe, Shoshiro; Sasaki, Yoshi N.; Terada, Mio
Citation	Journal of Oceanography, 72(6), 905-922 <a href="https://doi.org/10.1007/s10872-016-0390-0">https://doi.org/10.1007/s10872-016-0390-0</a>
Issue Date	2016-12
Doc URL	<a href="http://hdl.handle.net/2115/67768">http://hdl.handle.net/2115/67768</a>
Rights	The final publication is available at Springer via <a href="http://dx.doi.org/10.1007/s10872-016-0390-0">http://dx.doi.org/10.1007/s10872-016-0390-0</a>
Type	article (author version)
File Information	160702_LIU_manuscript_rev2_combined.pdf



[Instructions for use](#)

1 Dynamical downscaling of future sea-level change in the western North  
2 Pacific using ROMS

3  
4  
5 Zhao-Jun Liu<sup>1,2</sup>, Shoshiro Minobe<sup>1</sup>, Yoshi N. Sasaki<sup>1</sup>, and Mio Terada<sup>1</sup>

6  
7  
8 <sup>1</sup> *Department of Natural History Sciences, Graduate School of Science,*  
9 *Hokkaido University, Sapporo, Japan*

10 <sup>2</sup> *State Key Laboratory of Satellite Ocean Environment Dynamics, Second Institute of*  
11 *Oceanography, State Oceanic Administration, Hangzhou, China*

12  
13  
14  
15  
16 Corresponding author:

17 Zhao-Jun Liu

18 Phone: +86-571-86693289 Fax: +86-571-88839374

19 E-mail: zjliu@mail.sci.hokudai.ac.jp

20 Mail address: State Key Laboratory of Satellite Ocean Environment Dynamics,

21 Second Institute of Oceanography, State Oceanic Administration

22 36 Baochubei Road, Hangzhou, 310012, China

23  
24  
25  
26  
27  
28  
29  
30  
31  
32  
33  
34

35

36

37 **Abstract**

38       The future regional sea level (RSL) rise in the western North Pacific is investigated  
39 by dynamical downscaling with the Regional Ocean Modeling System (ROMS) with an  
40 eddy-permitting resolution based on three global climate models—MIROC-ESM,  
41 CSIRO-Mk3.6.0, and GFDL-CM3—under the highest greenhouse-gas emission  
42 scenario. The historical run is forced by the air-sea fluxes calculated from Coordinated  
43 Ocean Reference Experiment version 2 (COREv2) data. Three future  
44 runs—ROMS-MIROC, ROMS-CSIRO, and ROMS-GFDL—are forced with an  
45 atmospheric field constructed by adding the difference between the climate model  
46 parameters for the 21<sup>st</sup> and 20<sup>th</sup> century to fields in the historical run.

47       In all downscaling, the RSL rise along the eastern coast of Japan is generally half  
48 or less of the RSL rise maxima off the eastern coast. The projected regional (total) sea  
49 level rises along the Honshu coast during 2081–2100 relative to 1981–2000 are 19–25  
50 (98–104), 6–15 (71–80), and 8–14 (80–86) cm in ROMS-MIROC, ROMS-CSIRO, and  
51 ROMS-GFDL, respectively. The discrepancies of the RSL rise along the Honshu coast  
52 between the climate models and downscaling are less than 10 cm. The RSL changes in  
53 the Kuroshio Extension (KE) region in all downscaling simulations are related to the  
54 changes of KE (northward shift or intensification) with climate change.

55

56 **Keywords**

57 dynamical downscaling, regional sea level rise, western North Pacific, ROMS, CMIP5  
58 climate models, global warming

59

60 **1. Introduction**

61 Sea level rise due to global warming is one of the most important changes that the  
62 oceans will undergo. Global mean sea level has risen at a rate of  $3.2 \pm 0.4$  mm year<sup>-1</sup>  
63 over 1993–2012 based on satellite altimeter sea surface height (SSH) observations  
64 (Cazenave and Cozannet 2014). The recent Intergovernmental Panel on Climate Change  
65 (IPCC) Fifth Assessment Report (AR5) indicated that the global mean sea level rise in  
66 the 5% to 95% possibility range for the period 2081–2100 compared with 1986–2005 is  
67 likely to be 45 to 82 cm for the highest emission scenario Representative Concentration  
68 Pathway (RCP) 8.5 (Church et al. 2013).

69 Observational analysis (Bindoff et al. 2007; Cazenave and Cozannet 2014) and  
70 coupled climate models (Landerer et al. 2007; Yin et al. 2010; Yin 2012) indicate that  
71 sea level changes in response to a changing climate are not geographically uniform, and  
72 show substantial regionality. Based on the satellite records for 1993–2012, the sea level  
73 in the western tropical Pacific and eastern Indian Oceans increased much faster than the  
74 global mean. In the Atlantic, the sea level rose over the whole basin except for the Gulf  
75 Stream region in this period, whereas the sea level fell in the eastern tropical Pacific  
76 (Cazenave and Cozannet 2014). Using ensemble projections of 12 models of Coupled  
77 Model Intercomparison Project Phase 3 (CMIP3) under the Special Report on Emission  
78 Scenario A1B, Yin et al. (2010) calculated the dynamic sea level (sea level deviation  
79 from the geoid) during 2091–2100 relative to 1981–2000, and found dipole sea level  
80 rise patterns in the North Atlantic and North Pacific, and a belt-like pattern in the  
81 Southern Ocean. Furthermore, Yin (2012) analyzed 34 models of the Coupled Model  
82 Intercomparison Project Phase 5 (CMIP5) and found that there is overall consistency  
83 between the projections of regional sea level (RSL, the deviation of SSH from the  
84 global mean value) change by the end of the 21<sup>st</sup> century based on the CMIP5 and

85 CMIP3 models for similar scenarios. Major mechanisms for non-uniform dynamical sea  
86 level changes are surface wind changes and surface heat and freshwater flux changes.  
87 (Sakamoto et al. 2005; Sato et al. 2005; Lowe and Gregory 2006; Landerer et al. 2007;  
88 Yin et al. 2010; Suzuki and Ishii 2011a; Sueyoshi and Yasuda 2012; Zhang et al. 2014).

89 In response to global warming, the future sea level rise in the North Pacific will  
90 increase dramatically in the western subtropical gyre east of Japan (Yin et al. 2010; Yin  
91 2012; Sueyoshi and Yasuda 2012). The large sea level rise is related to changes in the  
92 Kuroshio Extension (KE), which has a steep meridional sea level gradient, or to larger  
93 heat uptake of water masses. Sasaki et al. (2014) recently showed the large sea level  
94 variability in the KE region in relation to meridional shifts of the KE jet on decadal  
95 timescales, based on tide-gauge and satellite-derived SSH data. Using an  
96 atmosphere-ocean coupled climate model, Sakamoto et al. (2005) showed a large sea  
97 level rise south of the KE associated with the intensification of the KE in response to  
98 global warming. In contrast, Sato et al. (2006) showed a large sea level rise east of  
99 Japan associated with a poleward shift of the KE by using a North Pacific ocean general  
100 circulation model. Sueyoshi and Yasuda (2012) analyzed 15 CMIP3 models and found  
101 that some models exhibit a larger northward shift of the KE, and that others exhibit a  
102 greater intensification of the KE. They further suggested that different projected  
103 changes in the wind stress caused by changes in atmospheric circulations over the North  
104 Pacific result in different responses of the KE, which characterize the different patterns  
105 of RSL rise in the western North Pacific. Suzuki and Ishii (2011a) investigated sea level  
106 changes caused by CO<sub>2</sub>-induced climate warming by using an atmosphere-ocean  
107 coupled climate model. They found that heat flux changes are more important than wind  
108 stress changes for the RSL rise in the southern recirculation of the KE in their model.

109 Suzuki and Ishii (2011b) decomposed baroclinic sea level changes based on the gridded  
110 observational data set into vertical modes, and found that the global warming signals are  
111 subducted into the ocean interior. This observation might be related to the formation of  
112 the North Pacific subtropical mode water around the KE region and the southern  
113 recirculation.

114 Japan is one of countries most likely to be affected by the sea level rise in the  
115 western North Pacific caused by global warming (Hanson et al. 2011). The Organization  
116 for Economic Co-operation and Development report (Nicholls et al. 2008) evaluated the  
117 risk of coastal cities over the world for future coastal flooding, and the Japanese cities  
118 Tokyo, Osaka-Kobe, and Nagoya are the 8<sup>th</sup>, 13<sup>th</sup>, and 17<sup>th</sup> cities measured by assets  
119 most exposed to coastal flooding in the 2070s, respectively. Therefore, there is a  
120 practical need for projections of RSL change caused by climate change along the  
121 Japanese coast.

122 However, the response of the Japanese coastal sea level to ocean circulation  
123 changes caused by global warming has not yet been adequately studied. Current climate  
124 models may not represent coastal sea level changes properly in the western North  
125 Pacific because the model resolutions are too coarse to resolve the narrow western  
126 boundary currents and the coastal topographies of islands. The most widely used  
127 approach to solve this problem is dynamical downscaling, which has recently been  
128 applied to projecting the effects of climate change on oceans (Meier 2006; Sato et al.  
129 2006; Ådlandsvik 2008; Sun et al. 2012; Chamberlain et al. 2012; Liu et al. 2013;  
130 Oliver et al. 2014; Seo et al. 2014; Liu et al. 2015). For example, Sato et al. (2006)  
131 conducted dynamical downscaling to study global warming-induced changes in North  
132 Pacific ocean circulations around Japan by using a North Pacific ocean general

133 circulation model driven by the sea surface flux derived from MRI-CGCM2.2, which is  
134 a climate model contributing to CMIP3. Their model covers the domain 15°S–65°N and  
135 100°E–75°W, with a horizontal resolution of 1/4° (zonally) and 1/6° (meridionally).  
136 They reported that coastal sea level rise along Japan is 12–18 cm (including the global  
137 mean thermal expansion of 10 cm, but ignoring land-ice melt etc.) from 2000 to 2070,  
138 smaller than the 40 cm sea level rise off the east of Japan. However, the spatial  
139 distribution of sea level changes along the Japanese coasts was not mentioned by Sato et  
140 al. (2006). Moreover, because they did not choose the climate model to be downscaled  
141 with a strategy for future sea level rise, it is not clear whether or not their results,  
142 obtained from downscaling of only one climate model, are representative. Different  
143 climate models produce different sea level changes (e.g., Sueyoshi and Yasuda 2012).  
144 Seo et al. (2014) performed dynamical downscaling for the North Pacific marginal seas,  
145 and thus their regional model covers the area 118°E–155°E and 18°N–50°N, which may  
146 be suitable for these marginal seas but not for the western North Pacific to the east of  
147 Japan. Therefore, downscaling of future RSL changes in the western North Pacific with  
148 an appropriate strategy is required. In this study, we examine future Japanese coastal  
149 RSL rise by dynamical downscaling with the Regional Ocean Modeling System  
150 (ROMS) based on CMIP5 models outputs. For proper representation of western  
151 boundary currents, which result from basin-scale atmospheric forcing, the ROMS  
152 domain should cover the whole zonal extent of the North Pacific basin, which is much  
153 wider than those in most previous downscaling studies (Meier 2006; Ådlandsvik 2008;  
154 Sun et al. 2012; Chamberlain et al. 2012; Liu et al. 2013; Oliver et al. 2014; Seo et al.  
155 2014; Liu et al. 2015). Dynamical downscaling involves a tradeoff between resolution  
156 and number of experiments because of the limitation of computational resources.

157 Therefore, we conduct downscaling of three CMIP5 models, which are selected to  
158 investigate the worst-case scenario. That is, we choose the three CMIP5 models that are  
159 likely to show the largest RSL rise around Japan to evaluate the upper limits of sea level  
160 rise.

161 The rest of the present paper is organized as follows. In Section 2, the CMIP5  
162 models used for the downscaling are selected, and the main features of the models are  
163 introduced. The methods used to generate the initial conditions, lateral boundary  
164 conditions, and the atmospheric forcing fields required for the ROMS are described. In  
165 Section 3, we compare the downscaled changes and those in the climate model  
166 projections and examine the RSL changes around Japan by the end of the 21<sup>st</sup> century.  
167 The summary and discussion are presented in Section 4.

168

## 169 2. Methods and Data

### 170 2.1 Global climate models

171 The CMIP5 climate model simulations used by the IPCC AR5 are mainly accessed  
172 through the Program for Climate Model Diagnosis and Intercomparison (PCMDI,  
173 website: <http://cmip-pcmdi.llnl.gov/cmip5/>). To project future climate change associated  
174 with increasing concentrations of greenhouse gases, the CMIP5 climate models were  
175 integrated under some RCP scenarios (Moss et al. 2010). To investigate the possible  
176 large sea level rise in the western North Pacific, we focus our attention on the highest  
177 emission scenario of RCP8.5 and climate models that have the highest RSL rise near  
178 Japan. This strategy will provide the worst-case scenario of RSL rise. Figure 1 shows  
179 the spatially averaged projected RSL change over a domain bounded by 25°N–40°N and  
180 125°E–180°E for the 2081–2100 period relative to the 1981–2000 period for 33 CMIP5

181 models under the RCP8.5 scenario. RSL is evaluated in this study because we are  
182 interested in the regional expression of sea level rise. This domain is used for the  
183 average because the region shows significant sea level rise in the multi-model ensemble  
184 mean from 34 models (Yin 2012). We select the three models with the largest  
185 area-averaged RSL rise, which are the MIROC-ESM, the CSIRO-Mk3.6.0, and the  
186 GFDL-CM3, as base models for the future dynamical downscaling.

187       The major features of the three CMIP5 models are as follows. In the MIROC-ESM,  
188 the ocean component is the Center for Climate System Research (University of Tokyo)  
189 Ocean Component Model (COCO 3.4). The longitudinal grid spacing is about  $1.4^\circ$ ,  
190 whereas the latitudinal grid intervals gradually vary from  $0.5^\circ$  at the equator to  $1.7^\circ$  near  
191 the North/South Poles (Watanabe et al. 2011). In CSIRO-Mk3.6.0, the ocean component  
192 is the Modular Ocean Model (MOM 2.2) with a horizontal resolution of  $1.875^\circ \times$   
193  $0.9375^\circ$  (Rotstayn et al. 2010; Jeffrey et al. 2013). The ocean model component of the  
194 GFDL-CM3 uses MOM4p1 code. The ocean model resolution is  $1^\circ$  for longitude. The  
195 meridional resolution gradually transitions from  $1/3^\circ$  at the equator to  $1^\circ$  at  $30^\circ\text{N}$  and  
196 remains as  $1^\circ$  between  $30^\circ\text{N}$  and  $65^\circ\text{N}$  in the Arctic (Griffies et al. 2005; Griffies et al.  
197 2011).

198

## 199 2.2 Regional ocean model

200       The present study uses ROMS to downscale and project sea level changes caused  
201 by climate change dynamically. The ROMS can be used for a diverse range of  
202 applications from local to planetary scales (e.g., Curchiser et al. 2005; Seo et al. 2007;  
203 Ådlandsvik 2008; Lorenzo et al. 2008; Han et al. 2009; Seo et al. 2014). The model  
204 solves the incompressible and hydrostatic primitive equations, and uses a free sea

205 surface on horizontally curvilinear coordinates and generalized terrain-following sigma  
206 vertical coordinates (Haidvogel et al. 2000; Shchepetkin and McWilliams 2005).

207 The model domain covers almost the entire North Pacific basin (110°E–100°W,  
208 5°N–50°N) with an eddy-permitting  $0.25^\circ \times 0.25^\circ$  horizontal resolution and 32 sigma  
209 levels in the vertical direction. The eddy-permitting model has biases, such as the  
210 Kuroshio Current overshooting northward along eastern coast of Japan (Shu et al. 2013)  
211 and northward shift of the KE (Sumata et al. 2012). Therefore, we examine biases in the  
212 model compared with observations, as described in Section 3.1, and consider the biases  
213 in interpreting the downscaled results.

214 Schemes used for boundary conditions and mixing are as follows. The radiation  
215 lateral boundary condition with nudging (time scale of 30-day) is used for temperature  
216 and salinity along the open boundaries at 5°N, 50°N, 110°E, and 100°W that permit  
217 long-term stable integration (Seo et al. 2007). A wall boundary condition is chosen for  
218 the sea surface elevation and the normal velocity. This is a zero gradient condition for  
219 surface elevation and zero flow for the normal velocity (Marchesiello et al. 2001).  
220 Harmonic horizontal mixing along an epineutral (constant density) surface is applied to  
221 the tracers, whereas biharmonic horizontal mixing along constant sigma surfaces is  
222 applied to the momentum. A third-order upstream horizontal advection scheme and  
223 fourth-order centered vertical advection scheme for momentum and tracer equations are  
224 used (Shchepetkin and McWilliams 2005). K-profile turbulence closure (Large et al.  
225 1994) is used for vertical mixing, and quadratic drag is applied to the bottom friction.

226

## 227 2.3 ROMS experiment settings

### 228 a. Historical run (1951–2000)

229 The historical run (ROMS-Hist) for the period 1951–2000 provides a reference for  
230 interpreting future run results. Initial salinity and potential temperature are set as the  
231 climatology of the World Ocean Atlas 2009 (WOA2009) (Locarnini et al. 2010;  
232 Antonov et al. 2010), and the initial sea level and velocities are set to zero. At the  
233 surface, the historical run is forced with six-hourly winds, air temperature, sea level  
234 pressure, specific humidity, daily mean downward shortwave and downward longwave  
235 radiation of the Coordinated Ocean Reference Experiment version 2 (COREv2) (Large  
236 and Yeager 2009) from 1951 to 2000. The primary data source of COREv2 data set is  
237 the NCEP/NCAR R1 reanalysis product, climatological biases in NCEP/NCAR R1 have  
238 been corrected in COREv2 on the basis of comparison with more reliable satellite and  
239 in situ measurements (Large and Yeager 2009). The effective ocean albedo is set to  
240 0.065 uniformly in the model domain, which is in the appropriate range of this domain.  
241 Upward longwave radiation is dependent on simulated sea surface temperature (SST).  
242 Surface wind stress and net heat fluxes are computed by using a bulk formula (Fairall et  
243 al. 2003). The model sea surface salinity is restored to the climatology values of CORE  
244 v2 data with a 30-day period. The lateral boundary values are provided from monthly  
245 mean Simple Ocean Data Assimilation version 2.2.4 (SODA 2.2.4) in the period from  
246 1951 to 2000 (Carton and Giese 2008).

247

#### 248 b. Future run (2051–2100)

249 Because CMIP5 models have biases in parameters that are used for momentum and  
250 heat flux calculations in downscaling in the present climate (Lee et al. 2013), the future  
251 run in the late 21<sup>st</sup> century is forced with atmospheric fields constructed by adding the  
252 monthly mean difference between the CMIP5 model parameters from the 21<sup>st</sup> and 20<sup>th</sup>

253 century to the observed parameters, which are mostly six-hourly, in the 20<sup>th</sup> century. The  
254 details of the approach are as follows. First, we calculate the monthly mean changes  
255 between 2051–2100 (RCP8.5) and 1951–2000 (CMIP5 historical) in each month and set  
256 of years (e.g., April 2079 minus April 1979) for the simulated winds, air temperature,  
257 relative humidity, sea level pressure, net shortwave and downward longwave radiation.  
258 Upward longwave radiation is dependent on simulated SST. Secondly, these monthly  
259 mean changes are added to CORE v2 atmospheric surface fields for the corresponding  
260 month and year for the 1951–2000 period used for ROMS-Hist. Finally, the bulk  
261 formula is used to calculate the projected surface fluxes of momentum, and sensible and  
262 latent heat, with the parameters determined in the second step. Similarly, the model sea  
263 surface salinity at each grid point is restored to the value that is given by the  
264 climatology used for historical run added 50-year time series of monthly sea surface  
265 salinity differences between 2051-2100 period and 1951-2000 period. We also apply  
266 this approach to the initial and lateral boundary conditions. The initial conditions for the  
267 future runs are also generated by adding the changes in temperature and salinity  
268 between January 1951 and January 2051 in the CMIP5 models to the initial condition of  
269 ROMS-Hist. The initial sea level and velocities are set to zero in all future runs. The  
270 lateral boundary conditions for the future runs are created by adding changes in monthly  
271 mean temperature, salinity, and velocity between 2051–2100 and 1951–2000 in the  
272 CMIP5 models to the respective fields in SODA 2.2.4 in the period 1951–2000. We call  
273 the three ROMS future runs forced by the MIROC-ESM, CSIRO-Mk3.6.0, and  
274 GFDL-CM3 variables ROMS-MIROC, ROMS-CSIRO, and ROMS-GFDL, respectively.  
275 The last 20 years of the historical run and of all future runs are used in the following  
276 analyses.

277

## 278 2.4 Regional sea level

279 To focus on the regional distribution, we analyze RSL, which is the sea level at  
 280 each grid point minus the global mean (e.g., Yin et al. 2010; Zhang et al. 2014). The  
 281 RSL in the CMIP5 models is given by

$$282 \quad h'_{CM}(x, y, t) = h_{CM}(x, y, t) - \bar{h}_{CM}^G(t) \quad (1)$$

283 where  $h_{CM}$  is the sea level in a climate model (zos in CMIP5),  $\bar{h}_{CM}^G$  is the global mean  
 284 sea level,  $t$  is time, and  $x$  and  $y$  are the zonal and meridional coordinates, respectively.  
 285 Because the ROMS domain does not cover the global, the RSL in ROMS simulations is  
 286 defined by

$$287 \quad h'_{ROMS}(x, y, t) = h_{ROMS}(x, y, t) - \bar{h}_{CM}^G(t) - (\bar{h}_{ROMS}^D(t) - \bar{h}_{CM}^D(t)) \quad (2)$$

288 where the  $h_{ROMS}$  is the sea level output of ROMS,  $\bar{h}_{CM}^G$  is the corresponding CMIP5  
 289 model's global mean,  $\bar{h}_{ROMS}^D$  and  $\bar{h}_{CM}^D$  are the means over the current model domain  
 290 (110°E–100°W, 5°N–50°N) in ROMS and the CMIP5 models, respectively.

291

## 292 2.5 Observational data

293 The ROMS-Hist is compared with the following observational data. The maps of  
 294 weekly absolute dynamic height are compiled from the TOPEX/Poseidon, ERS-1/2,  
 295 Jason-1, and Envisat altimeter observations on a  $1/3^\circ \times 1/3^\circ$  Mercator spatial resolution  
 296 grid from January 1993 to December 2000, distributed by the Archiving, Validation and  
 297 Interpretation of Satellite Oceanographic Data (AVISO) (Ducet et al. 2000). The  
 298 absolute dynamic height products are computed with consistent sea level anomaly and  
 299 mean dynamic topography field (Rio and Hernandez 2004).

300

301 

### 3. Results

302 

#### 3.1 Comparison of ROMS-Hist and observations

303 To evaluate the capability of the ROMS downscaling, the time-mean surface  
304 velocity obtained from the three CMIP5 models, ROMS-Hist, and satellite data are  
305 compared in Figure 3. Generally, all three CMIP5 models show a broad, weak Kuroshio  
306 Current and KE. It should be noted that ROMS-Hist fails to produce some observed  
307 features, as expected for an eddy-permitting model (e.g., Kagimoto and Yamagata 1997;  
308 Sumata et al. 2012; Shu et al. 2013). The KE is mainly formed roughly along 37°N with  
309 a minor eastward flow around 30°N. In the satellite observations, the Kuroshio Current  
310 separates from the coast and turns into the KE around 35°N. The modeled extension  
311 around 30°N is associated with the separation of the Kuroshio Current from the coast to  
312 the east of Kyushu. The systematic discrepancies between the ROMS-Hist and the  
313 observations should be considered in interpreting downscaled future changes.

314 The different surface current structures among the CMIP5 climate models,  
315 ROMS-Hist, and observation are reflected in differences in SSH, because the SSH  
316 gradient is closely related to the surface current speeds through the geostrophy. Figure 4  
317 shows that ROMS-Hist exhibits sharp SSH gradients across the Kuroshio Current and  
318 the KE as observed, although the CMIP5 climate models have broad, weak gradients  
319 especially over the KE. Proper reproduction of sharp SSH gradients is important in sea  
320 level changes, because shifts in SSH fronts can produce large sea level changes.

321 Another deficiency in the CMIP5 climate models is that the three straits connecting  
322 the Japan Sea either to the North Pacific Ocean or to marginal seas, such as the  
323 Tsushima, Tsugaru, and Soya Straits (Fig. 2), are not properly resolved. The Tsugaru

324 Strait is closed in MIROC-ESM and CSIRO-Mk3.6.0, whereas the Soya Strait is closed  
325 in GFDL-CM3. Therefore, examination of future flow changes through the straits is  
326 impossible using these climate models, but is possible using ROMS downscaling. The  
327 observed volume transports are 2.6 Sv ( $1 \text{ Sv} = 10^6 \text{ m}^3 \text{ s}^{-1}$ ) (Fukudome et al. 2010), 1.6  
328 Sv (Ito et al. 2003), and 0.7 Sv (Fukamachi et al. 2010) through the Tsushima, Tsugaru,  
329 and Soya Straits, respectively, whereas they are 2.6, 2.4, and 0.2 Sv in ROMS-Hist (Fig.  
330 15). Hence, ROMS-Hist represents the Tsushima Strait throughflow very well, whereas  
331 overestimates the Tsugaru Strait and underestimates the Soya Strait throughflow.

332

### 333 3.2 Regional sea level changes around Japan

334 In this section, we investigate how large the RSL changes around Japan are by the  
335 end of 21<sup>st</sup> century under the RCP8.5 scenario. Figure 5 shows the projected changes in  
336 mean RSL around Japan during 2081–2100 relative to 1981–2100 in the three CMIP5  
337 models and in the corresponding ROMS downscaling simulations. The three CMIP5  
338 models project RSL rises in the subtropical gyre east of Japan, with a maximal RSL rise  
339 of 44, 37, and 27 cm in MIROC-ESM, CSIRO-Mk3.6.0, and GFDL-CM3, respectively.

340 The RSL changes in the ROMS simulations have finer structures and higher  
341 magnitudes than those in the CMIP5 models, with some similarities among different  
342 downscaling simulations (Fig. 5). The ROMS downscaling exhibits larger RSL rise  
343 maxima than the CMIP5 models; the RSL rise maxima reach 63, 67, and 76 cm in  
344 ROMS-MIROC, ROMS-CSIRO, and ROMS-GFDL, respectively. The downscaled  
345 RSLs commonly exhibit zonally aligned three maxima along 37°N between 140°E and  
346 160°E. A comparison of these RSL rise patterns with the surface currents at the end of  
347 the 21<sup>st</sup> century (Fig. 6) and the end of the 20<sup>th</sup> century (Fig. 3) reveals that the RSL rise

348 along 37°N is associated with the northward shift of the KE in ROMS-MIROC and  
349 ROMS-GFDL. The relatively large RSL rise at 30°N and 40°N is related to the  
350 substantial weakening of the eastward current along 30°N found in ROMS-Hist and to  
351 the increased eastward currents around 40°N. It should be noted that in all ROMS  
352 simulations, RSL increases larger than 30 cm are limited to seaward of the continental  
353 shelf off the Japanese archipelago, so that the high off-shore RSL rise would not reach  
354 the coast of Japan.

355 To better understand the relationship between the off-shore and coastal RSL  
356 changes, we examine the meridional distribution of the RSL rise zonally averaged over  
357 145°E–155°E and that on the Japanese eastern coast simulated by the CMIP5 models  
358 (Fig. 7) and the ROMS downscaling (Fig. 8). We select the coastal RSL as the RSL at  
359 the ocean grid located next to the easternmost land grid of Japan at each latitude. In all  
360 CMIP5 models and ROMS simulations, the RSL changes along the eastern coast of  
361 Japan are generally half or less of the RSL rise maxima off the eastern coast of Japan.

362 Figure 9 shows RSL rises at all coastal grid points along Honshu Island, which is  
363 artificially connected to Kyushu and Shikoku islands forming one island in the ROMS  
364 simulations (Fig. 2), and Hokkaido Island. The coastal RSL changes during 2081–2100  
365 relative to 1981–2000 derived directly from the three CMIP5 models and those obtained  
366 from ROMS downscaling are shown in Figs. 9a and 9b for the eastern and western  
367 coasts, respectively. The projected RSL rises during 2081–2100 relative to 1981–2000  
368 along Honshu are 19–25, 6–15, and 8–14 cm in ROMS-MIROC, ROMS-CSIRO, and  
369 ROMS-GFDL, respectively. An important feature is that the differences in RSL changes  
370 between downscaling simulations and the corresponding CMIP5 models are less than 10  
371 cm along Honshu coast. This means that if a 10 cm discrepancy is allowed at the

372 maximum, we can use climate model outputs directly to assess the RSL rise along  
373 Honshu coast. The smaller differences in coastal RSL than in off-shore RSL between the  
374 ROMS downscaling and climate models are probably caused by coastally trapped shelf  
375 waves. These waves tend to average sea level along the coast, resulting in roughly  
376 constant coastal sea level, which is given by the average of sea level at the northern and  
377 southern ends of the island (Liu et al. 1999). Tsujino et al., (2008) successfully obtained  
378 semi-analytical solution of coastal sea-level around Japan arising through adjustment of  
379 coastal trapped waves and Rossby waves consistent with their OGCM of similar  
380 grid-spacing from the present model. We compared the simulated coastal sea levels and  
381 observed sea level anomalies averaged over 4 stations, which were selected by Japan  
382 Meteorological Agency for the most reliable long available stations, along the Japanese  
383 coast in the period of 1971–2000 ( $r=0.37$ , significant at the 95% confidence level).  
384 Therefore, the year-to-year variability of the model coastal sea level is consistent with  
385 that in the observed sea levels along the Japanese coast. The northward decrease in RSL  
386 changes on the western Honshu coast may be consistent with the northward propagation  
387 of shelf waves with damping along the route.

388         Although the RSL rises in the CMIP5 models and in ROMS downscaling are  
389 generally similar along Honshu, they can be substantially different at the islands  
390 separated from Honshu, because sea levels at those islands are not affected by the  
391 averaging effects of coastal waves. Here, we examine sea level change at Okinawa  
392 Island (Fig. 2), because extremely high sea levels have occurred there (Tokeshi and  
393 Yanagi 2003), suggesting that it is important to project the RSL rise at Okinawa Island  
394 in the future warming climate. Although Okinawa Island is too small to be represented  
395 as an island in the current ROMS downscaling simulations, sea level changes at the

396 island would be well approximated by the modeled sea level changes at that location.  
 397 Figure 10 shows the projected RSL changes at Okinawa Island during 2081–2100  
 398 relative to 1981–2000 in the three CMIP5 models and corresponding ROMS  
 399 simulations. Both ROMS-MIROC and ROMS-CSIRO project high RSL rises at  
 400 Okinawa Island of 29 and 32 cm, respectively, which are as much as or larger than the  
 401 RSL rise maxima on the Honshu coast. However, ROMS-GFDL projects relatively  
 402 small RSL rise at Okinawa Island of 9 cm. The difference between CSIRO-Mk3.6.0 and  
 403 ROMS-CSIRO is 16 cm, exceeding the aforementioned maximal discrepancy of 10 cm  
 404 along Honshu coast between the CMIP5 climate model and ROMS downscaling.

405

### 406 3.3 Three-dimensional oceanic changes

407 As revealed by previous studies, the spatial distributions of RSL rise in the western  
 408 North Pacific are related to the upper ocean changes (Sakamoto et al. 2005; Sato et al.  
 409 2006; Suzuki and Ishii 2011a; Sueyoshi and Yasuda 2012). In this section, we  
 410 investigate future changes below the surface in the western North Pacific to understand  
 411 the relationships between these changes and the RSL rise around Japan.

412 Sea level changes accompanied by density changes are represented by dynamic  
 413 height (DH). DH is a commonly used parameter that can be calculated in terms of  
 414 temperature and salinity by Eq. 3 (Gill 1982) with reference to 2000 dbar.

$$415 \quad \Delta DH = \frac{1}{g} \int_{2000}^0 (v_s(S, T, p) - v_s(35 \text{ psu}, 0 \text{ }^\circ\text{C}, p)) dp \quad (3)$$

416 Here,  $S$  is salinity,  $T$  is temperature,  $g$  is acceleration due to gravity, and  $v_s$  is specific  
 417 volume, given by the reciprocal of in situ density, and the anomaly of specific volume is  
 418 defined as the specific volume related to that at the same pressure for salinity of 35 psu  
 419 and temperature of 0 °C. Thus, DH is defined as the vertical integration of the specific

420 volume anomaly from the pressure of 2000 to 0 dbar (at the surface). For consistency  
 421 with the RSL rise, regional dynamic height (RDH) is defined in a similar manner to the  
 422 RSL definition (Eq. 2) as

$$423 \quad \Delta DH'_{ROMS} = \Delta DH_{ROMS} - \overline{\Delta DH}_{CM}^G - (\overline{\Delta DH}_{ROMS}^D - \overline{DH}_{CM}^D) \quad (4)$$

424 where the  $\Delta DH_{ROMS}$  is DH calculated by the ROMS outputs,  $\overline{\Delta DH}_{CM}^G$  is the  
 425 corresponding CMIP5 model's global mean DH,  $\overline{\Delta DH}_{ROMS}^D$  and  $\overline{\Delta DH}_{CM}^D$  are the DH  
 426 means over the North Pacific ROMS domain in ROMS and the CMIP5 models,  
 427 respectively.

428 Figure 11 shows the RDH changes during 2081–2100 relative to 1981–2000  
 429 obtained from the three ROMS downscaling simulations. The comparison of the RDH  
 430 changes (Figs. 11(a)–(c)) and RSL rises (Figs. 5(d)–(f)) indicate that the RDH changes  
 431 very well reproduce the major features of RSL rises described in the previous section,  
 432 including RSL rises associated with the KE changes.

433 We examine subsurface signatures related to RSL rises penetrate downward. Figure  
 434 12 shows projected changes in mean eastward velocity zonally averaged from 145°E to  
 435 155°E in a meridional-vertical cross section across the KE during 2081–2100 relative to  
 436 1981–2000 in the ROMS simulations. The zonal velocity changes are consistent with  
 437 the aforementioned KE changes. Velocity increase in ROMS-CSIRO is collocated with  
 438 the KE in the 20<sup>th</sup> century, indicating the KE intensification. In ROMS-GFDL, velocity  
 439 increases (decreases) to the north (south) of the KE axis in the 20<sup>th</sup> century, showing the  
 440 northward migration of the KE axis. In ROMS-MIROC, strong velocity increase is  
 441 found to the north of the 20<sup>th</sup> century KE axis but weak increase occur almost over the  
 442 whole KE axis, suggestive of the combination of the northward migration and overall  
 443 intensification. The zonal velocity changes mainly occur in the upper 1000 m, and

444 penetrate down to 2000 m in ROMS-GFDL. The vertical penetration may suggest that  
 445 this pattern is unlikely to be caused by heat or fresh water fluxes at the surface. This is  
 446 because such thermohaline flux changes would cause temperature and salinity changes  
 447 primarily limited to major water masses such as subtropical mode water at depths of  
 448 300–400 m or shallower (Suzuki and Ishii 2011b). Therefore, these changes are  
 449 probably forced by wind stress changes (e.g., Sakamoto et al. 2005; Sato et al. 2006;  
 450 Sueyoshi and Yasuda 2012). The velocity changes in ROMS-MIROC and  
 451 ROMS-CSIRO penetrate to a shallower depth than ROMS-GFDL. In addition, in  
 452 ROMS-CSIRO, near surface decrease of density is much more prominent than in the  
 453 other two models (not shown). These features in ROMS-CSIRO suggest that water mass  
 454 changes may play a more important role in the RSL in this model than in the others,  
 455 while both the effects of wind stress changes and water mass changes are all included in  
 456 ROMS-MIROC. Temperature changes penetrate to 2000 m, which is consistent with the  
 457 zonal velocity changes of the KE (Fig. 13), whereas the vertical penetration of the  
 458 salinity changes are limited to the upper 1000 m because of the lack of mean salinity  
 459 gradients deeper than 1000 m (not shown). All ROMS simulations commonly show that  
 460 the positive Sverdrup function changes east of Japan (Fig. 14) are caused by the  
 461 negative wind stress curl changes over the North Pacific (not shown).

462 The RDH changes shown in Figs. 11(a)–(c) are decomposed into thermosteric and  
 463 halosteric components. The decomposition methods are described in Eqs. (5) and (6)  
 464 (Landerer et al. 2007; Zhang et al. 2014).

$$465 \quad \Delta DH_T = \frac{1}{g} \int_{2000}^0 (v_s(35psu, T, p) - v_s(35 psu, 0^\circ C, p)) dp \quad (5)$$

$$466 \quad \Delta DH_S = \frac{1}{g} \int_{2000}^0 (v_s(S, 0^\circ C, p) - v_s(35 psu, 0^\circ C, p)) dp \quad (6)$$

467 Here,  $\Delta DH_T$  and  $\Delta DH_S$  are the thermosteric and halosteric DH, respectively. The  
468 calculation of regional thermosteric and halosteric DH is similar to that of RDH given  
469 in Eq. (4). Figures 11(d)–(f) and 11(g)–(i) show the regional thermosteric and halosteric  
470 contributions, respectively, to RDH changes during 2081–2100 relative to 1981–2000.  
471 The sum of these two components recover the RDH changes well (Figs. 11(j)–(l)). Thus,  
472 although the density is a nonlinear function of temperature, salinity and depth, its  
473 nonlinearity is weak with respect to temperature and salinity differences caused by the  
474 climate change. In all ROMS simulations, thermosteric components dominate the RDH  
475 change between 30°N and 40°N. Smaller halosteric components contribute to producing  
476 a larger RDH to the south than to the north. Consequently, the thermosteric component  
477 gives the major RDH, and thus the major RSL rise features, whereas the effect of  
478 halosteric component is small.

479 The spatial structure of the sea level changes may be associated with changes in the  
480 throughflow transport via the Tsugaru, Tsushima, and Soya Straits, because differences  
481 in sea level between the upstream and downstream of a strait strongly constrains  
482 throughflows (Ohshima 1994; Lyu and Kim 2005; Tsujino et al. 2008). Figure 15 shows  
483 the time-mean volume transports during 1981–2000 period and 2081–2100 period  
484 through the Tsushima, Tsugaru, and Soya Straits in ROMS downscaling. All transports  
485 through the straits will increase in the future warming climate. ROMS-CSIRO projects a  
486 much larger increase in the transports of each strait compared with the other two  
487 downscaling simulations. This is probably because ROMS-CSIRO projects a negative  
488 RSL rise in the subpolar gyre (Fig. 5), in contrast to the positive RSL rise in the other  
489 two models. The negative RSL rise in the subpolar gyre, combined with the positive  
490 RSL rise in the subtropical gyre is associated with the larger increase in SSH difference

491 between the subpolar and subtropical gyres in ROMS-CSIRO than in other two models.

492       Apart from the context of sea level rise, an interesting parameter in ROMS  
493 downscaling is SST, which is important in feedback from the ocean to the atmosphere  
494 (e.g., Small et al. 2008; Chelton and Xie 2010) and marine ecosystems (e.g.,  
495 Abdul-Aziz et al. 2011). Figures 16 (a)–(c) show that the three climate models exhibit  
496 the maximal SST increase to the east of the Tsugaru Strait, which suggests that the  
497 northward migration of the Kuroshio Current affects these models. The maximal SST  
498 warming in ROMS downscaling is reminiscent of the SST change in the climate model  
499 (Figs. 16(d)–(f)), as downscaling simulations also have maximal SST warming just east  
500 of the Tsugaru Strait. However, the magnitude of the maximal SST warming in  
501 ROMS-GFDL is as high as 11 °C, nearly 1.2 times larger than that in the corresponding  
502 climate model (9 °C). In addition, ROMS-CSIRO exhibits enhanced SST warming  
503 relative to the climate model, whereas maximal SST warming in ROMS-MIROC is only  
504 slightly larger than in the climate model. The localized maximal SST change is probably  
505 related to the larger northward intrusion of the Kuroshio Current at the end of the 21<sup>st</sup>  
506 century than that at the end of the 20<sup>th</sup> century in surface current velocities (Figs. 3 and  
507 6). The present downscaling model has a bias in the separation latitude of the Kuroshio  
508 Current from the eastern coast of Japan. However, the maximal SST increase around the  
509 northernmost latitude of the coastal Kuroshio Current in climate models and ROMS  
510 downscaling simulations suggests that future changes in the Kuroshio Current may  
511 result in large SST change around its separation latitude observed at about 35°N.

512

#### 513 4. Summary and discussion

514       We investigated the future RSL rise in the western North Pacific by conducting

515 dynamical downscaling by using ROMS with eddy-permitting  $0.25^\circ \times 0.25^\circ$  resolution.  
516 To evaluate the worst cases of RSL rise at the end of 21<sup>st</sup> century around Japan, we  
517 selected three climate models that have the highest RSL rise near Japan (Fig. 1),  
518 MIROC-ESM, CSIRO-Mk3.6.0, and GFDL-CM3, under the highest greenhouse-gas  
519 emission scenario, RCP8.5. The dynamical downscaling are performed for two epochs:  
520 the historical run (1950–2000) and the future run (2051–2100). The historical run,  
521 ROMS-Hist, is forced by the air-sea fluxes calculated by using COREv2 data. Three  
522 future runs—ROMS-MIROC, ROMS-CSIRO, and ROMS-GFDL—are forced with an  
523 atmospheric field constructed by adding the difference between the CMIP5 parameters  
524 of the 21<sup>st</sup> and 20<sup>th</sup> century to the present forcing fields used in ROMS-Hist.

525         The ROMS downscaling captures finer structures and stronger magnitudes for the  
526 RSL changes than those in the CMIP5 models. The downscaled changes commonly  
527 exhibit three zonally aligned maxima along  $37^\circ\text{N}$  between  $140^\circ\text{E}$  and  $160^\circ\text{E}$  (Fig. 5).  
528 The projected RSL rise maxima during 2081–2100 relative to 1981–2000 reach 63, 67,  
529 and 76 cm, in ROMS-MIROC, ROMS-CSIRO, and ROMS-GFDL, respectively (Fig.  
530 5).

531         All ROMS downscaling commonly show that the coastal RSL rises are smaller  
532 than the off-shore RSL rises (Figs. 5 and 8), consistent with Sato et al. (2006). The  
533 projected RSL rises along the Honshu coast during 2081–2100 relative to 1981–2000  
534 are 19–25, 6–15, and 8–14 cm in ROMS-MIROC, ROMS-CSIRO, and ROMS-GFDL,  
535 respectively, which are generally half or less of the RSL rise maxima off the eastern  
536 coast of Japan. Moreover, the ranges of RSL changes along the Honshu coast are small  
537 in all ROMS downscaling, probably due to shelf waves, which play a role in spatial  
538 averaging associated with wave's propagation along the coast (Fig. 9). Although the

539 CMIP5 models underestimate off-shore RSL rise maxima substantially than ROMS  
540 downscaling (Figs. 5, 7, and 8), the discrepancies between the climate models and  
541 ROMS downscaling are less than 10 cm along the Honshu coast (Fig. 9). Because the  
542 averaging effects of the shelf waves do not contribute to the sea level for islands  
543 separated from Honshu, larger RSL changes can occur for some islands than those along  
544 Honshu with larger differences between the climate models and ROMS downscaling. At  
545 Okinawa Island, the RSL changes are nearly 30 cm in ROMS-MIROC and  
546 ROMS-CSIRO, which is higher than the changes along the Honshu coast. The  
547 difference in RSL rise at Okinawa Island between ROMS-CSIRO and CSIRO-Mk3.6.0  
548 exceeds 10 cm (Fig. 10).

549 In ROMS-GFDL, the RSL changes to the east of Japan are accompanied by the  
550 zonal velocity changes across KE in the upper 1000 m, penetrating down to 2000 m  
551 (Fig. 12), probably due to wind stress changes (e.g., Sakamoto et al. 2005; Sato et al.  
552 2006; Sueyoshi and Yasuda 2012), whereas the shallow velocity and near surface  
553 density changes in ROMS-CSIRO suggests that water mass changes play a larger role  
554 than the other two models. Both the effects of wind stress and water mass changes are  
555 likely to be included in ROMS-MIROC. The RDH changes relative to 2000 dbar  
556 reproduce major features of RSL rises very well, including RSL rises associated with  
557 the KE changes mainly contributed by the thermosteric component rather than from the  
558 halosteric component (Fig. 11).

559 Other factors that are not taken into account in the present downscaling simulation  
560 can influence RSL changes, such as the inverse barometer effect, glacial isostatic  
561 adjustment (GIA), gravitational changes resulted from land ice melting and changes of  
562 land water storage, and climate model drift (Church et al. 2013; Slangen et al. 2014).

563 The inverse barometer effect, which yields an absolute sea level change less than 3 cm  
564 over the North Pacific in all models, is much smaller than the steric and land ice  
565 contributions and hence can be neglected. Based on the IPCC AR5, the GIA and  
566 gravitation changes has a relatively small effect around Japan. Climate drifts of the three  
567 CMIP5 climate models, which are evaluated using the pre-industry control run, are  
568 small for RSL in the western North Pacific, and can be ignored.

569 In order to obtain information useful for society, it is important to evaluate total sea  
570 level rise, which can be obtained by the RSL change through downscaling and the  
571 global mean sea level rise. Contributions to global mean sea level change include  
572 glaciers, land ice and land water storage contributions, thermal expansion contribution,  
573 and GIA (Church et al. 2013; Slangen et al. 2014). The GIA effect on the global mean  
574 sea level is small (-3 cm in 100 years) (Peltier and Luthcke 2009). The glaciers, land ice,  
575 and land water storage contributions to the global mean sea level rise are nearly 16, 16,  
576 and 4 cm, respectively, in 2081–2100 relative to 1986–2005 for RCP8.5 in IPCC AR5  
577 (Table 13.SM.1, Church et al. 2013). The thermal expansion components during 2081–  
578 2100 relative to 1981–2000 under RCP8.5 are 43, 29, and 36 cm, in MIROC-ESM,  
579 CSIRO-Mk3.6.0, and GFDL-CM3, respectively<sup>1</sup>. As a result, the global mean sea level  
580 rise are 79, 65, and 72 cm during 2081–2100 relative to 1981–2000 under RCP8.5 in  
581 MIROC-ESM, CSIRO-Mk3.6.0, and GFDL-CM3, as a minor reference period  
582 difference of 20<sup>th</sup> century, i.e., 1986–2005 in AR5 and 1980–2000 in the present study,  
583 can be ignored. Consequently, the coastal sea level rise in total, which is given by the

---

<sup>1</sup> Globally averaged sea-level due to thermal expansion (thermosteric component) is estimated with a variable, *zostoga*, in CMIP5. However, *zostoga* is not available for GFDL-CM3, and thus we use another variability, *zossga*, (global average steric sea level change). For MIROC-ESM, both *zostoga* and *zossga* are available and the difference between them are small (less than 0.3% for 100 year difference).

584 addition of the RSL increase documented in section 3.2 and the global mean sea level  
585 rise, are expected to be 101–108, 73–80, and 80–90 cm in MIROC-ESM,  
586 CSIRO-Mk3.6.0, and GFDL-CM3, respectively.

587 An important result in the present study is that the present downscaling reveals that  
588 the discrepancy along the Honshu coast between the CMIP5 climate models and  
589 corresponding ROMS downscaling is less than 10 cm. Thus, with 10 cm uncertainty, the  
590 RSL change along the Honshu coast can be directly evaluated from CMIP5 climate  
591 model outputs. This allows the coastal RSL rise to be evaluated with a larger number of  
592 climate models (nearly 40), and the probability of sea level changes to be evaluated  
593 considering the uncertainties among climate models.

594 At the eddy-permitting  $0.25^\circ \times 0.25^\circ$  resolution here, ROMS-Hist exhibits some  
595 bias, such as the overshoot of the Kuroshio Current and the northward shift of KE  
596 compared with observations. Although we have taken these biases into account in  
597 interpreting the downscaled sea level changes, it is not possible to identify the specific  
598 locations and magnitudes of the largest coastal sea level rise. To overcome these biases,  
599 downscaling with eddy-resolving resolution of  $0.1^\circ \times 0.1^\circ$  may be required. This should  
600 be an important research in future, because Tokyo, the most densely city and the capital  
601 of Japan, is located near from the separation point of the Kuroshio at  $35^\circ\text{N}$ . The  
602 computational cost of this resolution is about 16 times larger than that in our  
603 experiments, which we expect will become feasible for a number of laboratories in the  
604 next decade.

605

## 606 Acknowledgments

607 We thank for fruitful discussion with Dr. Tamaki Yasuda and Dr. Tatsuo Suzuki.

608 This work was supported by JSPS KAKENHI Grant Numbers 26287110, 26610146,  
609 15H01606. The numerical calculations were carried out on a computer in the Institute of  
610 Low Temperature Science, Hokkaido University.

611

## 612 References

613 Abdul-Aziz OI, Mantua NJ, Myers KW (2011) Potential climate change impacts on  
614 thermal habitats of Pacific salmon (*Oncorhynchus* spp.) in the North Pacific Ocean  
615 and adjacent seas. *Can J Fish Aquat Sci* 68(9):1660-1680. doi: 10.113/F2011-079

616 Ådlandsvik B (2008) Marine downscaling of a future climate scenario for the North Sea.  
617 *Tellus* 60A:451-458. doi: 10.1111/j.1600-0870.2008.00311.x

618 Antonov JI, Seidov D, Boyer TP, Locarnini RA, Mishonov AV, Garcia HE, Baranova  
619 OK, Zweng MM, Johnson DR (2010) World Ocean Atlas 2009. In: Levitus S (eds)  
620 Vol. 2. Salinity, NOAA Atlas NESDIS 68, Government Printing Office, Washington,  
621 pp. 184

622 Bindoff NL et al (2007) Observations: Oceanic climate change and sea level. In:  
623 Solomon S et al (eds) *Climate Change 2007: The Physical Science Basis*.  
624 Contribution of Working Group I to the Fourth Assessment Report of the  
625 Intergovernmental Panel on Climate Change, Cambridge University Press,  
626 Cambridge

627 Carton JA, Giese BS (2008) A reanalysis of ocean climate using Simple Ocean Data  
628 Assimilation (SODA), *Mon Weather Rev* 136(8):2999-3017

629 Cazenave A, Cozannet GL (2013) Sea level rise and its coastal impacts. *Earth's Future*  
630 2:15-34. doi: 10.1002/2013EF000188

631 Chamberlain MA, Sun CJ, Matear RJ, Feng M, Phipps SJ (2012) Downscaling the

- 632 climate change for oceans around Australia. *Geosci Model Dev* 5:1177-1194
- 633 Chelton DB, Xie SP (2010) Coupled ocean-atmosphere interaction at oceanic  
634 mesoscales. *Oceanog* 23(4):52-69
- 635 Church JA et al (2013) Sea Level Change. In: Stocker TF et al (eds) *Climate Change*  
636 2013: The Physical Science Basis. Contribution of Working Group I to the Fifth  
637 Assessment Report of the Intergovernmental Panel on Climate Change, Cambridge  
638 University Press, Cambridge
- 639 Curchitser EN, Haidvogel DB, Hermann AJ, Dobbins EL, Powell TM, Kaplan A (2005)  
640 Multi-scale modeling of the North Pacific Ocean: Assessment and analysis of  
641 simulated basin-scale variability (1996-2003). *J Geophys Res* 110(C11021). doi:  
642 10.1029/2005JC002902
- 643 Ducet N, Le Traon PY, Reverdin G (2000) Global high resolution mapping of ocean  
644 circulation from TOPEX/Poseidon and ERS-1/2. *J Geophys Res* 105(19):477-498
- 645 Fairall CW, Bradley EF, Hare JE, Grachev AA, Edson JB (2003) Bulk parameterization  
646 of air-sea fluxes: Updates and verification for the COARE algorithm. *J Clim*  
647 16:571-591
- 648 Fukamachi Y, Ohshima KI, Ebuchi N, Bando T, Ono K, Sano M (2010) Volume  
649 transport in the Soya strait during 2006-2008. *J Oceanogr* 66:685-696
- 650 Fukudome K, Yoon JH, Ostrovskii A, Takikawa T, Han IS (2010) Seasonal volume  
651 transport variation in the Tsushima warm current through the Tsushima Straits from  
652 10 years of ADCP observations. *J Oceanogr* 66:539-551
- 653 Gill AE (1982) *Atmosphere-ocean dynamics*. Academic Press, Harcourt Place, London,  
654 pp. 215
- 655 Griffies SM et al (2005) Formulation of an ocean model for global climate simulations.

- 656 Ocean Sci 1:45-79
- 657 Griffies SM, Winton M, Donner LJ et al (2011) The GFDL CM3 coupled climate  
658 model: Characteristics of the ocean and sea ice simulations. *J Clim* 24:3520-3544.  
659 doi: 10.1175/2011JCLI3964.1
- 660 Haidvogel DB, Arango HG, Hedstrom K, Beckmann A, Malanotte-Rizzoli P,  
661 Shchepetkin AF (2000) Model evaluation experiments in the North Atlantic  
662 basin: Simulations in nonlinear terrain-following coordinates. *Dyn Atmos Oceans*  
663 32:239-281
- 664 Han W, Moore AM, Levin J, Zhang B, Arango HG, Curchitser E, Lorenzo ED, Gordon  
665 AL, Lin J (2009) Seasonal surface ocean circulation and dynamics in the Philippine  
666 Archipelago region during 2004-2008. *Dyn Atmos Oceans* 47:114-137
- 667 Hanson S, Nicholls R, Ranger N, Hallegatte S, Corfee-Morlot J, Herweijer C, Chateau J  
668 (2011) A global ranking of port cities with high exposure to climate extremes. *Clim*  
669 *Change* 104:89-111. doi: 10.1007/s10584-010-9977-4
- 670 Ito T, Togawa O, Ohnishi M, Isoda Y, Nakayama T, Shima S, Kuroda H, Iwahashi M,  
671 Sato C (2003) Variation of velocity and volume transport of the Tsugaru warm  
672 current in the winter of 1999-2000. *Geophys Res Lett* 30(13):1678.  
673 doi:10.1029/2003GL017522
- 674 Jeffrey SJ, Rotstayn L, Collier M, Dravitzk S, Hamalaien C, Moeseneder C, Wong K,  
675 Syktus J (2013) Australia's CMIP5 submission using the CSIRO Mk3.6 model.  
676 *Aust Meteorol Oceanogr J* 63:1-13
- 677 Kagimoto T, Yamagata T (1997) Seasonal transport variations of the Kuroshio: An  
678 OGCM simulation. *J Phys Oceanogr* 27:403-418.
- 679 Landerer FW, Jungclaus JH, Marotzke J (2007) Regional dynamic and steric sea level

- 680 change in response to the IPCC=A1B scenario. *J Phys Oceanogr* 37:296-312
- 681 Large WG, McWilliams JC, Doney SC (1994) Oceanic vertical mixing: A review and a  
682 model with a nonlocal boundary layer parameterization. *Rev Geophys* 32:363-404
- 683 Large WG, Yeager S (2009) The global climatology of an interannually varying air-sea  
684 flux data set. *Clim Dyn* 33:341-364. doi: 10.1007/s00382-008-0441-3
- 685 Lee T, Waliser DE, Li JF, Landerer FW, Gierach MM (2013) Evaluation of CMIP3 and  
686 CMIP5 wind stress climatology using satellite measurements and atmospheric  
687 reanalysis products. *J Clim* 26:5810-5826. doi: 10.1175/JCLI-D-12-00591.1
- 688 Liu Y, Xie L, Morrison JM, Kamykowski D (2013) Dynamic downscaling of the impact  
689 of climate change on the ocean circulation in the Galápagos Archipelago. *Adv*  
690 *Meteorol* 2013:1-18
- 691 Liu Y, Lee SK, Enfield DB, Muhling BA, Lamkin JT, Muller-Karger FE, Roffer MA  
692 (2015) Potential impact of climate change on the Intra-Americas Sea: Part-1. A  
693 dynamic downscaling of the CMIP5 model projections. *J Mar Sys* 148(2015):56-69
- 694 Liu Z, Wu L (1999) Rossby wave-coastal kelvin wave interaction in the extratropics.  
695 part II: Formation of island circulation. *J Phys Oceanogr* 29:2405-2418
- 696 Locarnini RA, Mishonov AV, Antonov JI, Boyer TP, Garcia HE, Baranova OK, Zweng  
697 MM, Johnson DR (2010) World Ocean Atlas 2009. In: Levitus S (eds) Vol. 1.  
698 Temperature, NOAA Atlas NESDIS 68, Government Printing Office, Washington,  
699 pp. 184
- 700 Lorenzo ED, Schneider N, Cobb KM, Franks PJS, Chhak K et al (2008) North Pacific  
701 gyre oscillation links ocean climate and ecosystem change. *Geophys Res Lett*  
702 35(L08607)
- 703 Lowe JA, Gregory M (2006) Understanding projections of sea level rise in a Hadley

- 704 Centre coupled climate model. *J Geophys Res* 111(C11014). doi:  
705 10.1029/2005JC003421
- 706 Lyu SJ, Kim K (2005) Subinertial to interannual transport variations in the Korea Strait  
707 and their possible mechanisms. *J Geophys Res* 110(C1206). doi: 10.1029/2004JC002651
- 708 Marchesiello P, McWilliams JC, Shchepetkin A (2001) Open boundary conditions for  
709 long-term integration of regional oceanic model. *Ocean Modell* 3:1-20
- 710 Meier HEM (2006) Baltic Sea climate in the late twenty-first century: A dynamical  
711 downscaling approach using two global models and two emission scenarios. *Clim  
712 Dyn* 27(1):39-68. doi: 10.1007/s00382-006-0124-x
- 713 Moss RH, Edmonds JA, Hibbard KA et al (2010) The next generation of scenarios for  
714 climate change research and assessment. *Nature* 463:747-756.  
715 doi:10.1038/nature08823
- 716 Nicholls RJ, Hanson S, Herweijer C, Patmore N, Hallegatte S et al (2008) Ranking port  
717 cities with high exposure and vulnerability to climate extremes: exposure estimates.  
718 OECD Publishing. <http://dx.doi.org/10.1787/011766488208>
- 719 Ohshima KI (1994) The flow system in the Japan Sea caused by a sea level difference  
720 through shallow straits. *J Geophys Res* 99:9925-9940
- 721 Oliver ECJ, Holbrook NJ (2014) Extending our understanding of South Pacific gyre  
722 “spin-up”: Modeling the East Australian Current in a future climate. *J Geophys Res  
723 Ocean* 119:2788-2805. doi: 10.1002/2013JC009591
- 724 Peltier WR, Luthcke SB (2009) On the origins of Earth rotation anomalies: New  
725 insights on the basis of both “paleogeodetic” data and Gravity Recovery and  
726 Climate Experiment (GRACE) data. *J Geophys Res* 114(B11405).  
727 doi:10.1029/2009JB006352

- 728 Rio MH, Hernandez F (2004) A mean dynamic topography computed over the world  
729 ocean from altimetry, in situ measurements, and a geoid model. *J Geophys Res*  
730 109(C12032). doi:10.1029/2003JC002226
- 731 Rotstayn LD et al (2010) Improved simulation of Australian climate and ENSO-related  
732 rainfall variability in a global climate model with an interactive aerosol treatment.  
733 *Int J Climatol* 30:1067-1088. doi: 10.1002/joc.1952
- 734 Sakamoto TT, Hasumi H, Ishii M, Emori S, Suzuki T, Nishimura T, Sumi A (2005)  
735 Responses of the Kuroshio and the Kuroshio Extension to global warming in a  
736 high-resolution climate model. *Geophys Res Lett* 32(L14617).  
737 doi:10.1029/2005GL023384
- 738 Sasaki YN, Minobe S, Miura Y (2014) Decadal sea-level variability along the coast of  
739 Japan in response to ocean circulation changes. *J Geophys Res Oceans* 119:266-275.  
740 doi: 10.1002/2013JC009327
- 741 Sato Y, Yukimoto S, Tsujino H, Ishizaki H, Noda A (2006) Response of North Pacific  
742 ocean circulation in a Kuroshio-resolving ocean model to an Arctic Oscillation  
743 (AO)-like change in Northern Hemisphere atmospheric circulation due to  
744 greenhouse-gas forcing. *J Meteorol Soc Jpn* 84:295-309
- 745 Sen Gupta A, Jourdain NC, Brown JN, Monselesan D (2013) Climate drift in the  
746 CMIP5 models. *J Clim* 26:8597-8615. doi: 10.1175/JCLI-D-12-00521.1
- 747 Seo H, Miller AJ, Roads JO (2007) The scripps coupled ocean-atmosphere regional  
748 (SCOAR) model, with applications in the eastern Pacific sector. *J Clim* 20:381-402
- 749 Seo GH, Cho YK, Choi BJ, Kim KY, Kim BG, Tak YJ (2014) Climate change  
750 projection in the Northwest Pacific marginal seas through dynamic downscaling. *J*  
751 *Geophys Res Oceans* 119:3497-3516. doi: 10.1002/2013JC009646

- 752 Shchepetkin AF, McWilliams JC (2005) The regional oceanic modeling system  
753 (ROMS): A split-explicit, free-surface, topography-following-coordinate ocean  
754 model. *Ocean Modell* 9:347-404
- 755 Shu Q, Qian FL, Song ZY, Yin XQ (2013) A comparison of two global ocean-ice  
756 coupled models with different horizontal resolutions. *Acta Oceanol Sin* 32(8):1-11
- 757 Small RJ, deSzoeko SP, Xie SP, O'Neill L, Seo H, Song Q, Cornillon P, Spall M,  
758 Minobe S (2008) Air-sea interaction over ocean fronts and eddies. *Dyn Atmos*  
759 *Oceans* 45:274-319. doi: 10.1016/j.dynatmoce.2008.01.001
- 760 Sueyoshi M, Yasuda T (2012) Inter-model variability of projected sea level changes in  
761 the western North Pacific in CMIP3 coupled climate models. *J Oceanogr*  
762 68:533-543. doi: 10.1007/s10872-012-0117-9
- 763 Sumata H, Hashioka T, Suzuki T, Yoshie N, Okunishi T, Aita MN, Sakamoto TT, Ishida  
764 A, Okada N, Yamanaka Y (2010) Effect of eddy transport on the nutrient supply  
765 into the euphotic zone simulated in an eddy-permitting ocean ecosystem model. *J*  
766 *Mar Sys* 83(2010):67-87. doi:10.1016/j.jmarsys.2010.07.002
- 767 Sun CJ, Feng M, Matear RJ, Chamberlain MA, Craig P, Ridgway KR, Schiller A (2012)  
768 Marine downscaling of a future climate scenario for Australian boundary currents. *J*  
769 *Clim* 25(8):2947-2962. doi: 10.1175/JCLI-D-11-00159.1
- 770 Suzuki T, Ishii M (2011a) Regional distribution of sea level changes resulting from  
771 enhanced greenhouse warming in the Model for Interdisciplinary Research on  
772 Climate version 3.2. *Geophys Res Lett* 38(L02601). doi:10.1029/2010GL045693
- 773 Suzuki T, Ishii M (2011b) Long-term regional sea level changes due to variations in  
774 water mass density during the period 1981-2007. *Geophys Res Lett* 38(L21604).  
775 doi: 10.1029/2011GL049326

- 776 Tokeshi T, Yanagi T (2003) High sea level caused at Naha in Okinawa Island. *Oceanogr*  
777 *Japan* 12(4):395-405 (**in Japanese with English abstract**)
- 778 Tsujino H, Nakano H, Motoi T (2008) Mechanism of currents through the straits of the  
779 Japan Sea: Mean state and seasonal variation. *J Oceanogr* 64:141-161
- 780 Watanabe S, Hajima T, Sudo K et al (2011) MIROC-ESM 2010: model description and  
781 basic results of CMIP5-20c3m experiments. *Geosci Model Dev* 4:845-872.  
782 doi:10.5194/gmd-4-845-2011
- 783 Yin J, Griffies SM, Stouffer RJ (2010) Spatial variability of sea level rise in twenty-first  
784 century projections. *J Clim* 23:4585-4607. doi:10.1175/2010JCLI3533.1
- 785 Yin J (2012) Century to multi-century sea level rise projections from CMIP5 models.  
786 *Geophys. Res Lett* 39(L17709). doi:10.1029/2012GL052947
- 787 Zhang XB, Church JA, Platten SM, Monselesan D (2014) Projection of subtropical gyre  
788 circulation and associated sea level changes in the Pacific based on CMIP3 climate  
789 models. *Clim Dyn* 43:131-144. doi:10.1007/s00382-013-1902-x
- 790
- 791
- 792
- 793
- 794
- 795
- 796
- 797
- 798
- 799

800

801

802 Figure Captions

803

804 Fig. 1 Projected RSL rises averaged over a domain bounded by 25°–40°N and 125°–  
805 180°E during 2081–2100 relative to 1981–2000 for 33 CMIP5 climate models. The  
806 three selected models are highlighted in red

807

808 Fig. 2 Topography around Japan from ROMS. Contours indicate bathymetric depths in  
809 meters, and gray areas indicate the land mask. Blue lines denote the locations of the  
810 Tsushima, Tsugaru, and Soya Straits. Red dots denote the costal stations used in Figure  
811 9 and the Okinawa Island station (26.75°N, 128°E) in Figure 10

812

813 Fig. 3 Time-mean surface velocities (colors) and vector velocities (vectors) for 1993–  
814 2000 in the three selected CMIP5 climate models (a–c), the ROMS historical run (d),  
815 and the satellite-derived surface geostrophic currents (e)

816

817 Fig. 4 Time-mean RSL for 1993–2000 period in three CMIP5 climate models (a–c), the  
818 ROMS historical run (d), and the satellite observations (e)

819

820 Fig. 5 Projected changes in mean RSL around Japan for 2081–2100 relative to 1981–  
821 2000 in (left) CMIP5 climate models under the RCP8.5 scenario and in (right) ROMS  
822 downscaling simulations. Top, middle, and bottom panels are for MIROC-ESM,  
823 CSIRO-Mk3.6.0, and GFDL-CM3, respectively

824

825 Fig. 6 Time-mean surface absolute velocities (colors) and vector velocities (vectors)  
826 averaged over 2081–2100 in (a) ROMS-MIROC, (b) ROMS-CSIRO, and (c)  
827 ROMS-GFDL

828

829 Fig. 7 (top) RSL zonally averaged from 145°E to 155°E and temporally averaged for  
830 1981–2000 (blue) and 2081–2100 (red), and (bottom) projected RSL rise zonally  
831 averaged from 145° to 155°E (black) and projected Japanese eastern coastal RSL rise  
832 (purple) for 2081–2100 relative to 1981–2000 in (left) MIROC-ESM, (middle)  
833 CSIRO-Mk3.6.0, and (right) GFDL-CM3

834

835 Fig. 8 (top) RSL zonally averaged from 145°E to 155°E and temporally averaged for  
836 1981–2000 (blue) and 2081–2100 (red), and (bottom) projected RSL rise zonally  
837 averaged from 145° to 155°E (black) and projected Japanese eastern coastal RSL rise  
838 (purple) for 2081–2100 relative to 1981–2000 for the ROMS downscaling simulations  
839 with (left) ROMS-MIROC, (middle) ROMS-CSIRO, and (right) ROMS-GFDL

840

841 Fig. 9 Projected Japanese eastern (a) and western (b) coastal RSL rise for 2081–2100  
842 relative to 1981–2000 in three CMIP5 models (triangles) and from ROMS simulations  
843 (dots), with MIROC-ESM and ROMS-MIROC (blue), CSIRO-Mk3.6.0 and  
844 ROMS-CSIRO (purple), and GFDL-CM3 and ROMS-GFDL (green). The labels A–D  
845 and A'–D' correspond to the location of the red dots shown in Fig. 2

846

847 Fig. 10 Projected RSL rise (in centimeters) at Okinawa Island (26.75°N, 128°E, as

848 shown in Fig. 2) during 2081–2100 relative to 1981–2000 in MIROC-ESM,  
849 CSIRO-Mk3.6.0, and GFDL-CM3 (black bars), and in the corresponding ROMS  
850 downscaling simulations (blue bars)

851

852 Fig. 11 (a–c) RDH changes with reference to 2000 dbar during 2081–2100 relative to  
853 the 1981–2000 period, (d–f) RDH changes due to the thermosteric component, and (g–i)  
854 RDH changes due to halosteric components, and (j–l) the sum of the thermosteric and  
855 halosteric components, in (left) ROMS-MIROC, (middle) ROMS-CSIRO, and (right)  
856 ROMS-GFDL

857

858 Fig. 12 Projected changes in mean eastward velocity zonally averaged from 145°E  
859 to 155°E for 2081–2100 relative to 1981–2000 (colors) in (a) ROMS-MIROC, (b)  
860 ROMS-CSIRO, and (c) ROMS-GFDL. Contours show the mean distribution for 1981–  
861 2000. The contour interval is 0.05 m/s

862

863 Fig. 13 Projected changes in potential temperature (in °C, color shading, meridional  
864 average has been removed at each depth) zonally averaged from 145°E to 155°E for  
865 2081–2100 relative to 1981–2000 in (a) ROMS-MIROC, (b) ROMS-CSIRO, and (c)  
866 ROMS-GFDL along with their mean value for 1981–2000 (contours). The contour  
867 interval is 3°C

868

869 Fig. 14 Projected changes in Sverdrup stream function (Sv, color shading) for 2081–  
870 2100 period relative to 1981–2000 period along with their mean value for 1981–2000  
871 (contours) in (a) ROMS-MIROC, (b) ROMS-CSIRO, and (c) ROMS-GFDL. Contours

872 interval is 15Sv

873

874 Fig. 15 Time-mean volume transports (in Sv) through (a) Tsushima, (b) Tsugaru, and (c)  
875 Sōya Strait for 1981–2000 (black) and 2081–2100 (blue) simulated by ROMS  
876 downscaling

877

878 Fig. 16 Projected SST change (°C) for 2081–2100 and 1981–2000 in (top) the CMIP5  
879 models and in (bottom) ROMS downscaling simulations for (left) MIROC-ESM,  
880 (middle) CSIRO-Mk3.6.0, and (right) GFDL-CM3, respectively

881

882

883

884

885

886

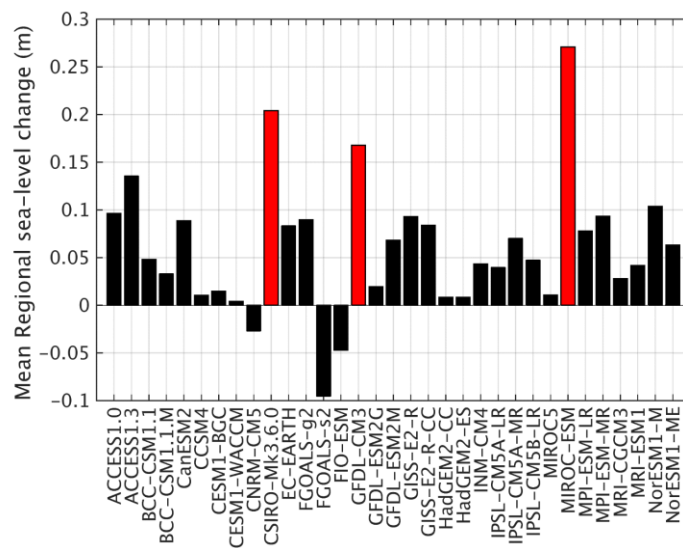
887

888

889

890

891



892

893

894

895

896

897

898

899

900

901

902

903

904

905

Fig. 1 Projected RSL rises averaged over a domain bounded by 25°–40°N and 125°–180°E during 2081–2100 relative to 1981–2000 for 33 CMIP5 climate models. The three selected models are highlighted in red.

906

907

908

909

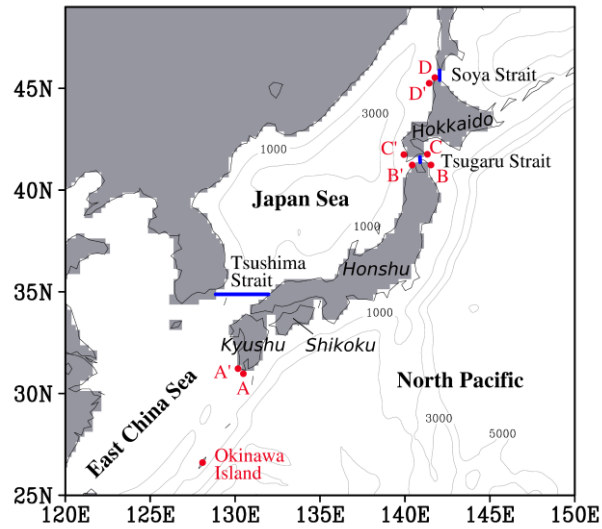
910

911

912

913

914



915

916 Fig. 2 Topography around Japan from ROMS. Contours indicate bathymetric depths in

917 meters, and gray areas indicate the land mask. Blue lines denote the locations of the

918 Tsushima, Tsugaru, and Soya Straits. Red dots denote the coastal stations used in Figure

919 9 and the Okinawa Island station (26.75°N, 128°E) in Figure 10.

920

921

922

923

924

925

926

927

928

929

930

931

932

933

934

935

936

937

938

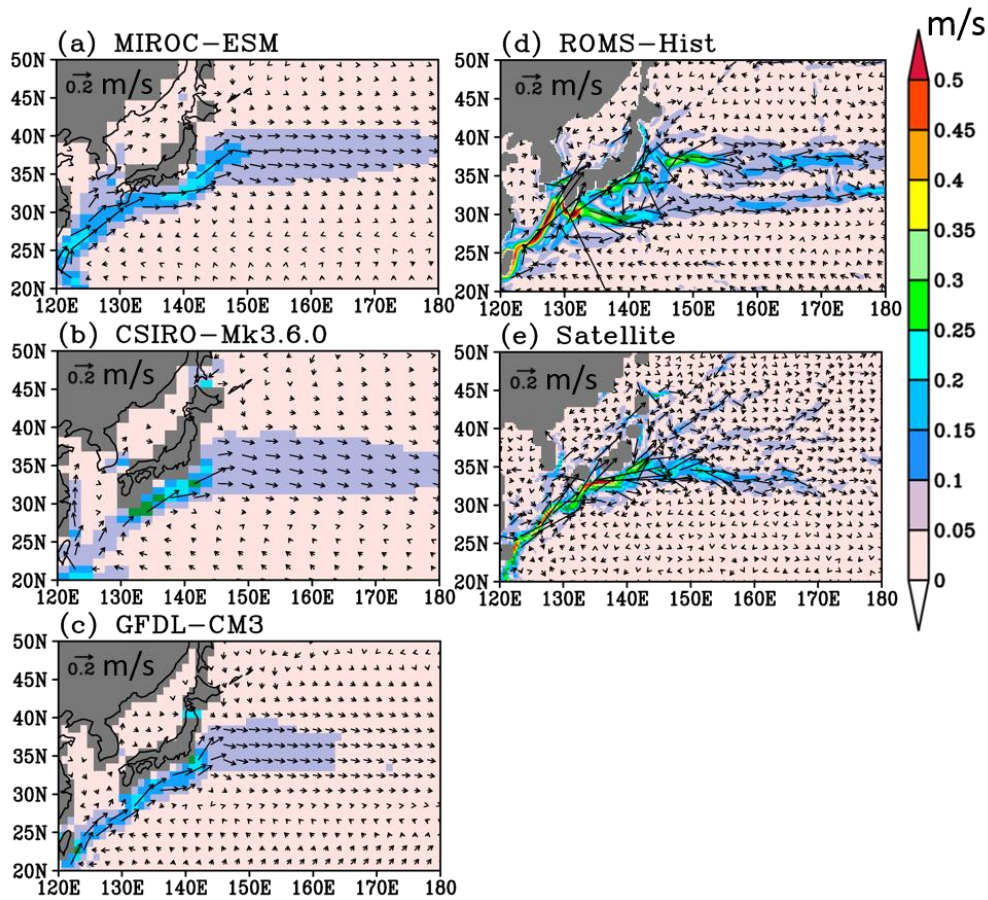
939

940

941

942

943



944

945

946

947

948

949

950

951

952

953

Fig. 3 Time-mean surface velocities (colors) and vector velocities (vectors) for 1993–2000 in the three selected CMIP5 climate models (a–c), the ROMS historical run (d), and the satellite-derived surface geostrophic currents (e).

954

955

956

957

958

959

960

961

962

963

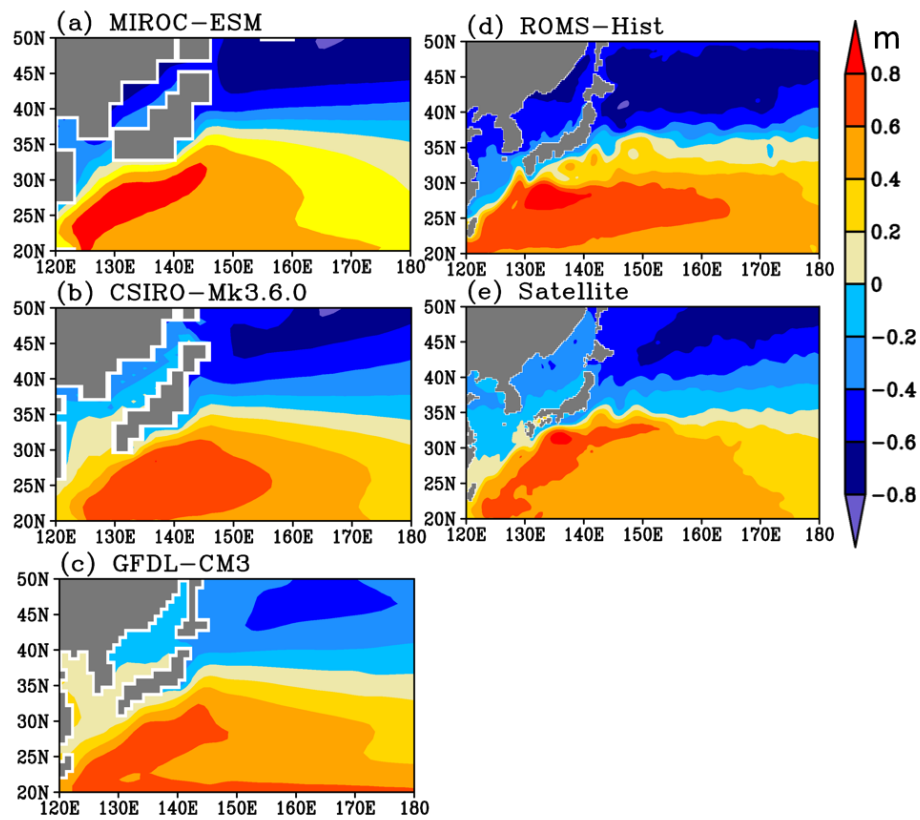
964

965

966

967

968



969 Fig. 4 Time-mean RSL for 1993–2000 period in three CMIP5 climate models (a–c), the

970 ROMS historical run (d), and the satellite observations (e).

971

972

973

974

975

976

977

978

979

980

981

982

983

984

985

986

987

988

989

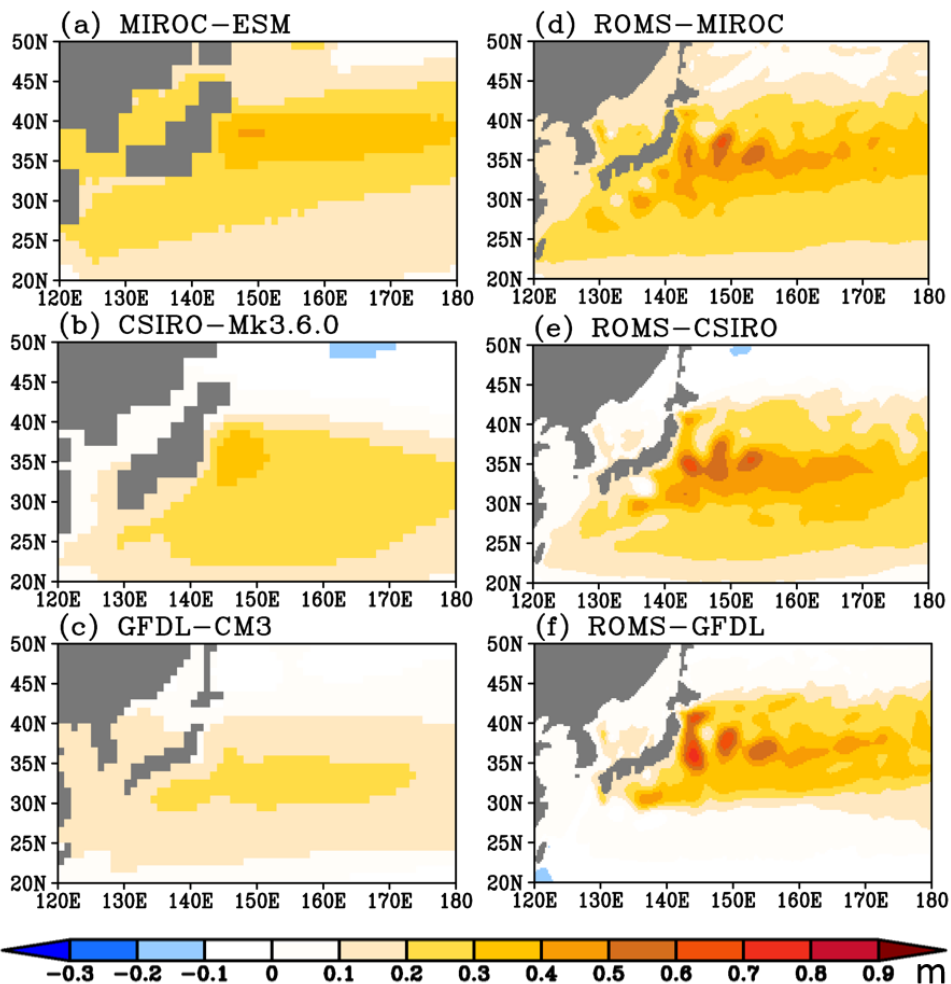
990

991

992

993

994



995 Fig. 5 Projected changes in mean RSL around Japan for 2081–2100 relative to 1981–

996 2000 in (left) CMIP5 climate models under the RCP8.5 scenario and in (right) ROMS

997 downscaling simulations. Top, middle, and bottom panels are for MIROC-ESM,

998 CSIRO-Mk3.6.0, and GFDL-CM3, respectively.

999

1000

1001

1002

1003

1004

1005

1006

1007

1008

1009

1010

1011

1012

1013

1014

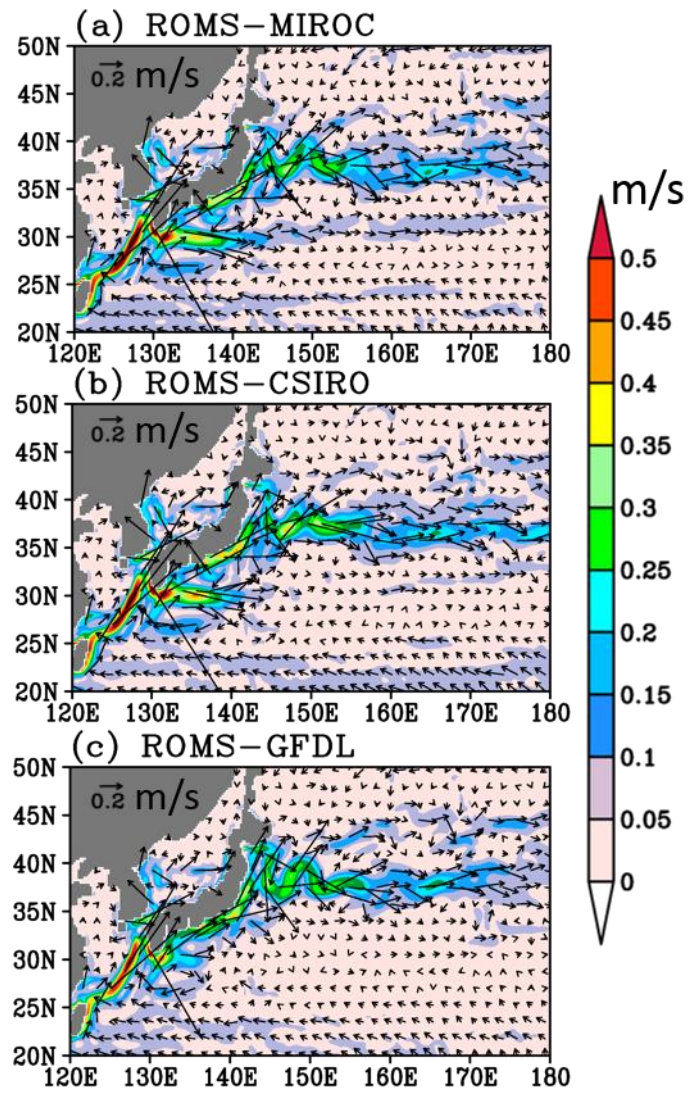
1015

1016

1017

1018

1019



1020 Fig. 6 Time-mean surface absolute velocities (colors) and vector velocities (vectors)

1021 averaged over 2081–2100 in (a) ROMS-MIROC, (b) ROMS-CSIRO, and (c)

1022 ROMS-GFDL.

1023

1024

1025

1026

1027

1028

1029

1030

1031

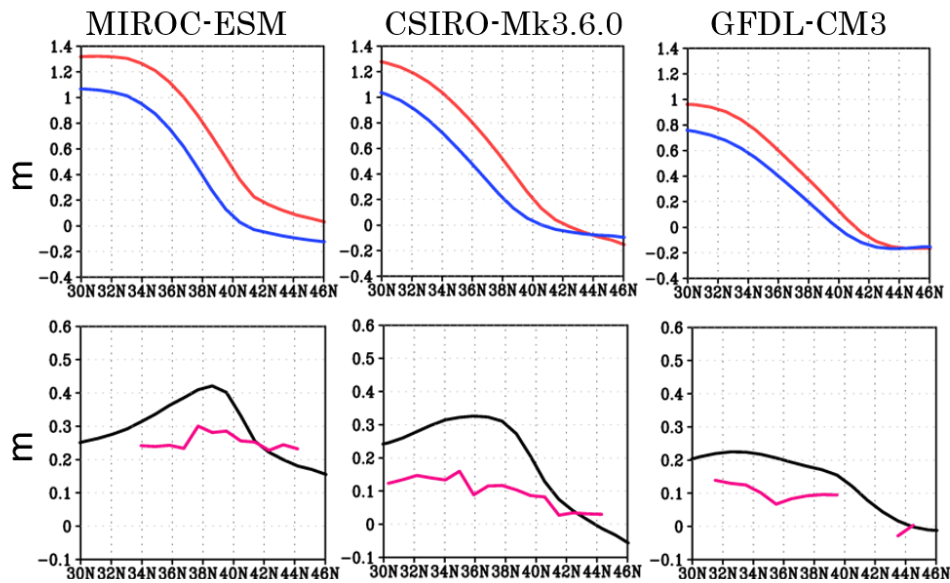
1032

1033

1034

1035

1036



1037 Fig. 7 (top) RSL zonally averaged from 145°E to 155°E and temporally averaged for  
 1038 1981–2000 (blue) and 2081–2100 (red), and (bottom) projected RSL rise zonally  
 1039 averaged from 145° to 155°E (black) and projected Japanese eastern coastal RSL rise  
 1040 (purple) for 2081–2100 relative to 1981–2000 in (left) MIROC-ESM, (middle)  
 1041 CSIRO-Mk3.6.0, and (right) GFDL-CM3.

1042

1043

1044

1045

1046

1047

1048

1049

1050

1051

1052

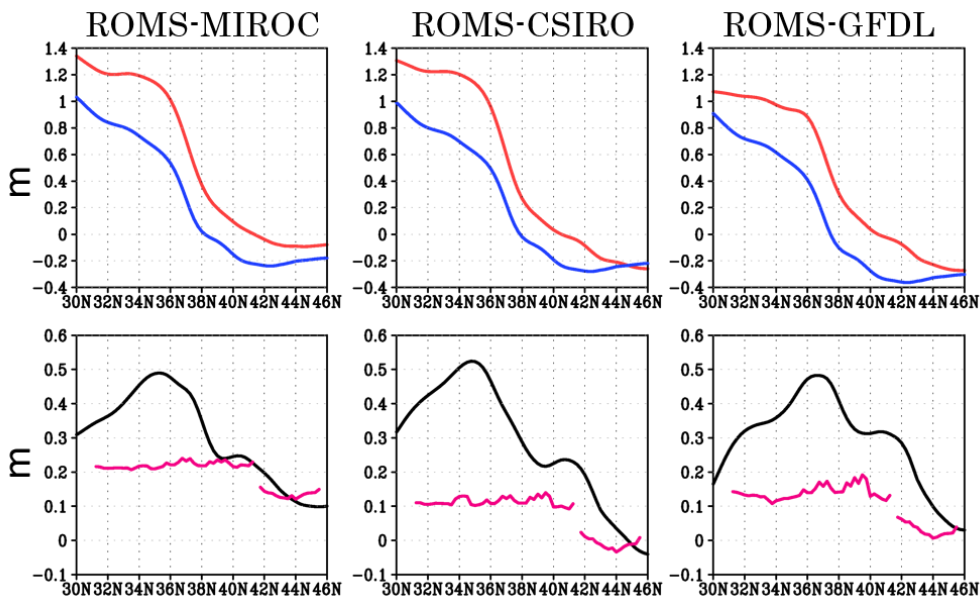
1053

1054

1055

1056

1057



1058

1059

1060

1061

1062 Fig. 8 (top) RSL zonally averaged from 145°E to 155°E and temporally averaged for

1063 1981–2000 (blue) and 2081–2100 (red), and (bottom) projected RSL rise zonally

1064 averaged from 145° to 155°E (black) and projected Japanese eastern coastal RSL rise

1065 (purple) for 2081–2100 relative to 1981–2000 for the ROMS downscaling simulations

1066 with (left) ROMS-MIROC, (middle) ROMS-CSIRO, and (right) ROMS-GFDL.

1067

1068

1069

1070

1071

1072

1073

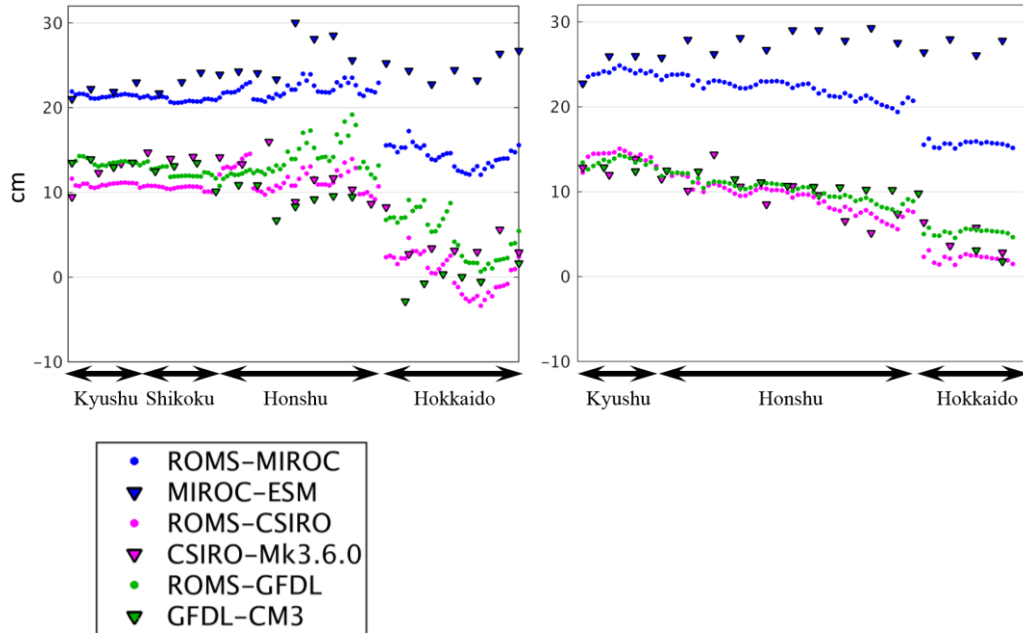
1074

1075

1076

1077

1078



1079

1080

1081

1082

1083

1084

1085

1086

1087

1088

1089

1090

1091

Fig. 9 Projected Japanese eastern (a) and western (b) coastal RSL rise for 2081–2100 relative to 1981–2000 in three CMIP5 models (triangles) and from ROMS simulations (dots), with MIROC-ESM and ROMS-MIROC (blue), CSIRO-Mk3.6.0 and ROMS-CSIRO (purple), and GFDL-CM3 and ROMS-GFDL (green). The labels A–D and A'–D' correspond to the location of the red dots shown in Fig. 2.

1092

1093

1094

1095

1096

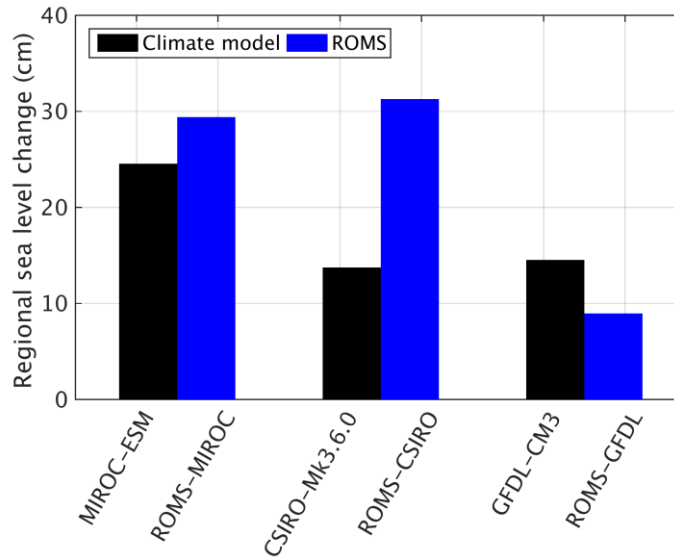
1097

1098

1099

1100

1101



1102 Fig. 10 Projected RSL rise (in centimeters) at Okinawa Island (26.75°N, 128°E, as

1103 shown in Fig. 2) during 2081–2100 relative to 1981–2000 in MIROC-ESM,

1104 CSIRO-Mk3.6.0, and GFDL-CM3 (black bars), and in the corresponding ROMS

1105 downscaling simulations (blue bars).

1106

1107

1108

1109

1110

1111

1112

1113

1114

1115



1140

1141

1142

1143

1144

1145

1146

1147

1148

1149

1150

1151

1152

1153 Fig. 12 Projected changes in mean eastward velocity zonally averaged from 145°E

1154 to 155°E for 2081–2100 relative to 1981–2000 (colors) in (a) ROMS-MIROC, (b)

1155 ROMS-CSIRO, and (c) ROMS-GFDL. Contours show the mean distribution for 1981–

1156 2000. The contour interval is 0.05 m/s.

1157

1158

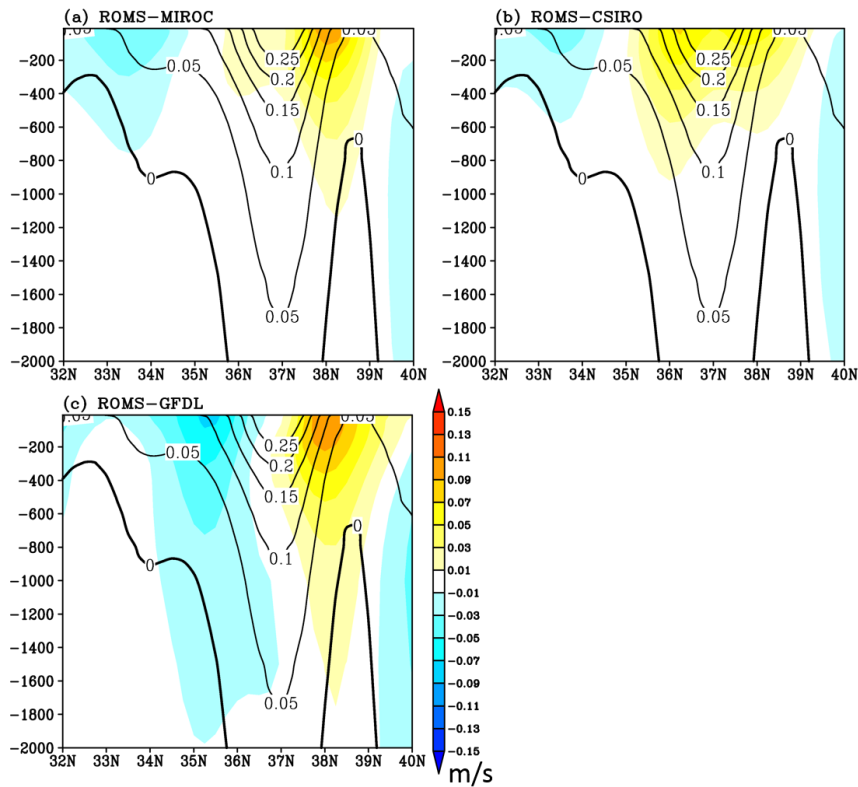
1159

1160

1161

1162

1163



1164

1165

1166

1167

1168

1169

1170

1171

1172

1173

1174

1175

1176

1177 Fig. 13 Projected changes in potential temperature (in °C, color shading, meridional  
 1178 average has been removed at each depth) zonally averaged from 145°E to 155°E for  
 1179 2081–2100 relative to 1981–2000 in (a) ROMS-MIROC, (b) ROMS-CSIRO, and (c)  
 1180 ROMS-GFDL along with their mean value for 1981–2000 (contours). The contour  
 1181 interval is 3 °C.

1182

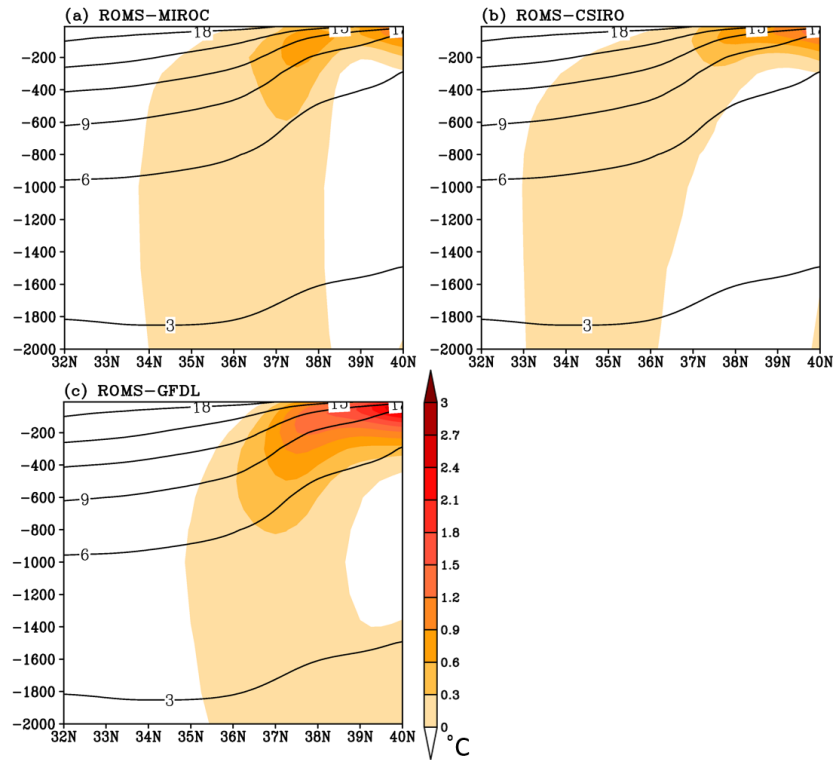
1183

1184

1185

1186

1187



1188

1189

1190

1191

1192

1193

1194

1195

1196

1197

1198

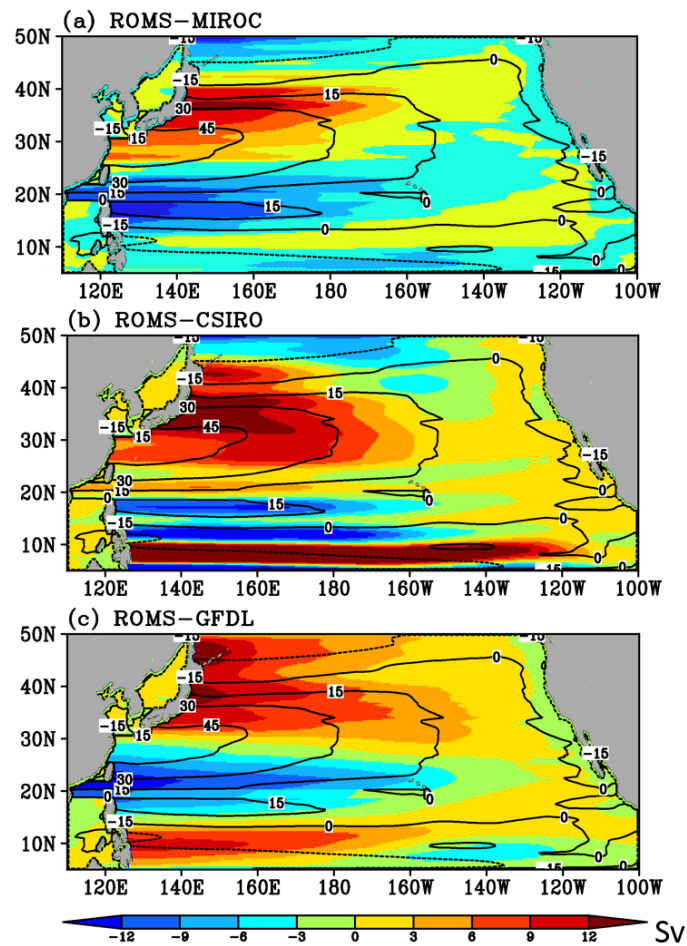
1199

1200

1201

1202

1203



1204 Fig. 14 Projected changes in Sverdrup stream function (Sv, color shading) for 2081–

1205 2100 period relative to 1981–2000 period along with their mean value for 1981–2000

1206 (contours) in (a) ROMS-MIROC, (b) ROMS-CSIRO, and (c) ROMS-GFDL. Contours

1207 interval is 15Sv.

1208

1209

1210

1211

1212

1213

1214

1215

1216

1217

1218

1219

1220

1221

1222

1223

1224

1225

1226 Fig. 15 Time-mean volume transports (in Sv) through (a) Tsushima, (b) Tsugaru, and (c)

1227 Sōya Strait for 1981–2000 (black) and 2081–2100 (blue) simulated by ROMS

1228 downscaling.

1229

1230

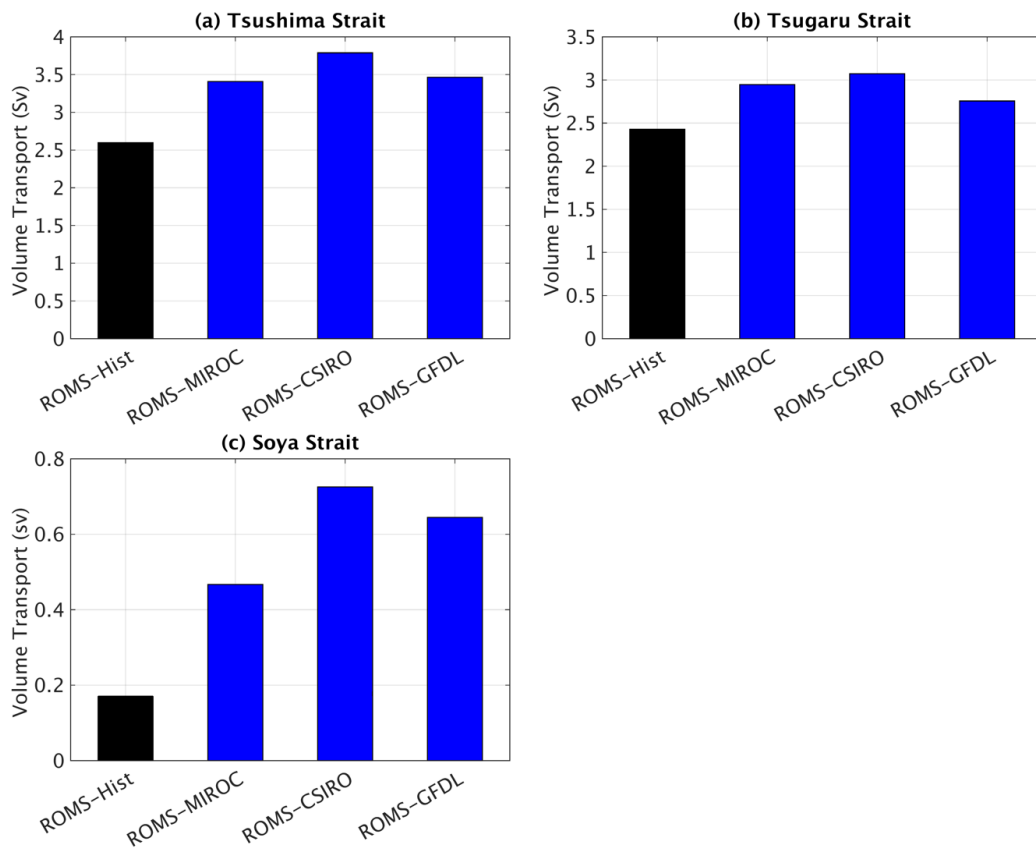
1231

1232

1233

1234

1235



1236

1237

1238

1239

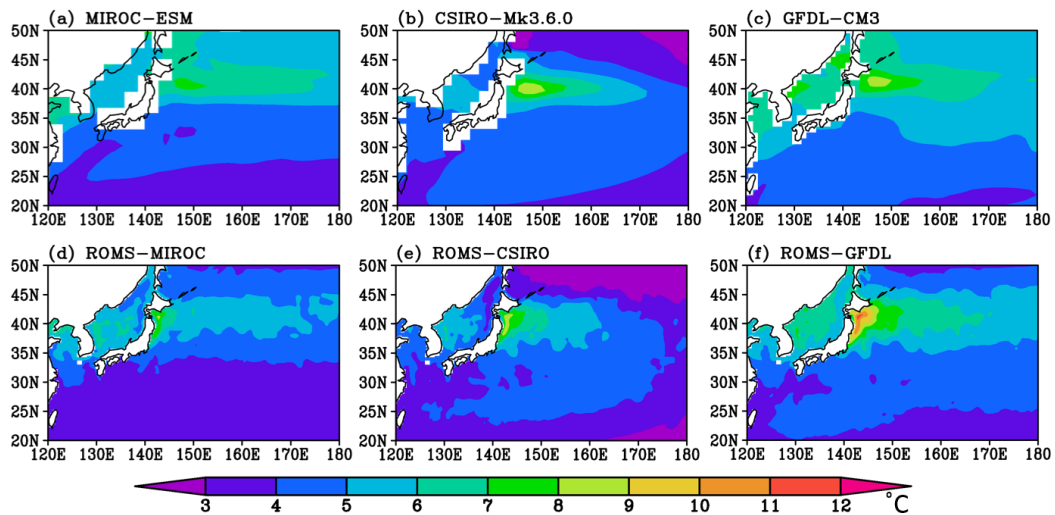
1240

1241

1242

1243

1244



1245

1246 Fig. 16 Projected SST change ( $^{\circ}\text{C}$ ) for 2081–2100 and 1981–2000 in (top) the CMIP5

1247 models and in (bottom) ROMS downscaling simulations for (left) MIROC-ESM,

1248 (middle) CSIRO-Mk3.6.0, and (right) GFDL-CM3, respectively.

1249

1250

1251

1252

1253

1254

1255

1256

1257

1258

1259

1260

1261

1262

1263

1264

1265

1266

1267

1268

1269

1270